

# ERRSat User Manual

John Xun Yang

## Contents

<b>1</b>	<b>Introduction</b>	<b>3</b>
1.1	Context . . . . .	3
1.2	ERRSat Overview . . . . .	4
<b>2</b>	<b>Download and Installation</b>	<b>5</b>
2.1	Download . . . . .	5
2.2	Installation . . . . .	5
2.3	Code Directory . . . . .	5
2.4	Ancillary Input Files . . . . .	7
2.5	Third Party Models . . . . .	7
<b>3</b>	<b>How to Use ERRSat</b>	<b>7</b>
3.1	A Quick Start . . . . .	7
3.2	Setting Error Sources . . . . .	8
3.3	Setting Modes . . . . .	10
3.4	Output and Visualization . . . . .	11
3.5	Advanced Setting . . . . .	11
<b>4</b>	<b>Observation Error Inventory</b>	<b>14</b>
4.1	Algorithm Basis . . . . .	14
4.2	Measurement error . . . . .	14
4.2.1	Radiometer diagram . . . . .	14
4.2.2	Generating count and $T_A$ with noise and orbital oscillation . . . . .	14
4.2.3	Windowing, calibration . . . . .	18
4.2.4	Decomposing Noise . . . . .	19
4.2.5	Cross-pol Contamination . . . . .	20
4.2.6	Twist angle offset . . . . .	22
4.2.7	Spacecraft attitude and geolocation . . . . .	25
4.2.8	Antenna pattern . . . . .	25
4.2.9	Faraday rotation . . . . .	25
4.2.10	Cross-polarization leakage . . . . .	27
4.2.11	Reflector emission . . . . .	27
4.2.12	Cold-space mirror emission . . . . .	28
4.2.13	Warm load error . . . . .	28
4.2.14	FOV intrusion . . . . .	28
4.2.15	Bandpass spectral response . . . . .	29

4.2.16	Interference of instrumental and geomagnetic field . . . . .	29
4.2.17	Crosstalk . . . . .	29
4.2.18	Count to antenna temperature . . . . .	30
4.2.19	Antenna temperature to brightness temperature . . . . .	31
4.3	Observation operator error . . . . .	31
4.3.1	Ancillary models and modules . . . . .	31
4.4	Representativeness error . . . . .	31
4.5	Pre-processing Error . . . . .	31
<b>A</b>	<b>Acronyms and Abbreviations</b>	<b>32</b>
<b>B</b>	<b>List of Error Sources</b>	<b>33</b>
<b>C</b>	<b>List of Scripts</b>	<b>34</b>

# 1 Introduction

## 1.1 Context

The error and uncertainty quantification associated with satellite observations are critical for hardware development, data assimilation, weather forecast, and environmental and climate data records [Kalnay, 2003; Langland and Baker, 2004; Joo et al., 2013; Geer et al., 2018]..

In the context of data assimilation, observation errors encompass four categories in terms of measurement error, observation operator error, representativeness error, and pre-processing error. In data assimilation requires quantifying observation error with error covariance for weighing different observations and models [Hollingsworth and Lönnberg, 1986; Desroziers et al., 2005; Stewart et al., 2014; Bormann and Bauer, 2010]. For instance, a number of methods have been developed to diagnose inter-channel correlation and its error covariance. Accounting inter-channel correlation can improve data assimilation against the counterpart of using uncorrelated error covariance [Weston et al., 2014; Janjić et al., 2018].

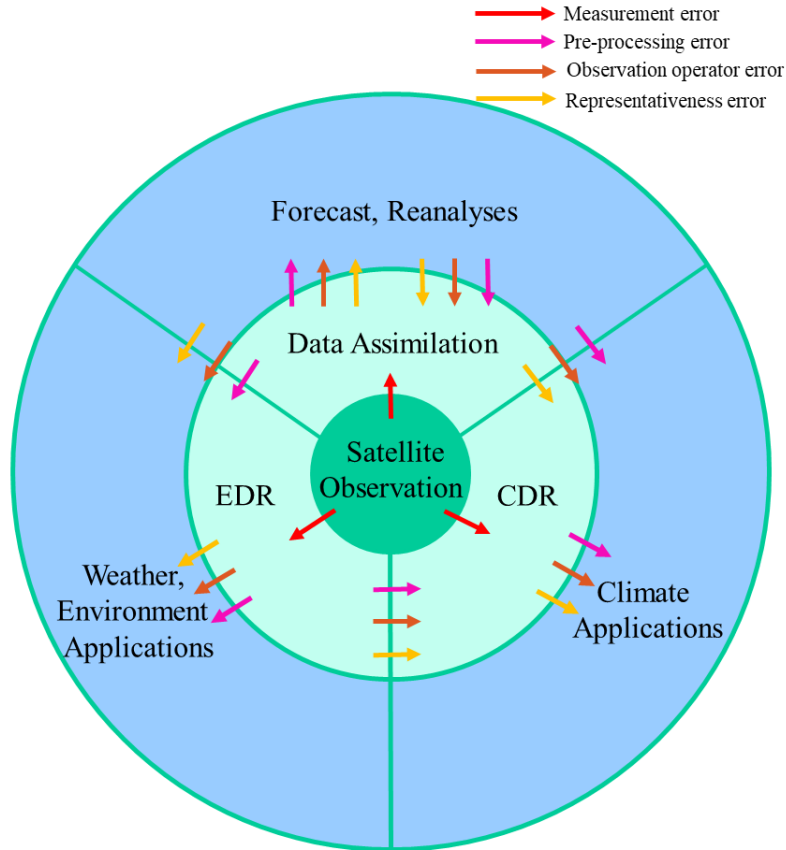


Figure 1: Comparison of the top-down and bottom-up approaches for observation uncertainty quantification. The error inventory ERRSat is a bottom-up approach.

Aside from data assimilation, assessing observation error and uncertainty also matters for the development and application of the Environmental Data Record (EDR) and Climate Data Record (CDR) from satellite observations [Hollmann et al., 2013; Ablain et al., 2015; Merchant et al., 2017; Bellprat et al., 2017; Merchant et al., 2019; Gruber et al., 2020]. An accurate uncertainty estimate

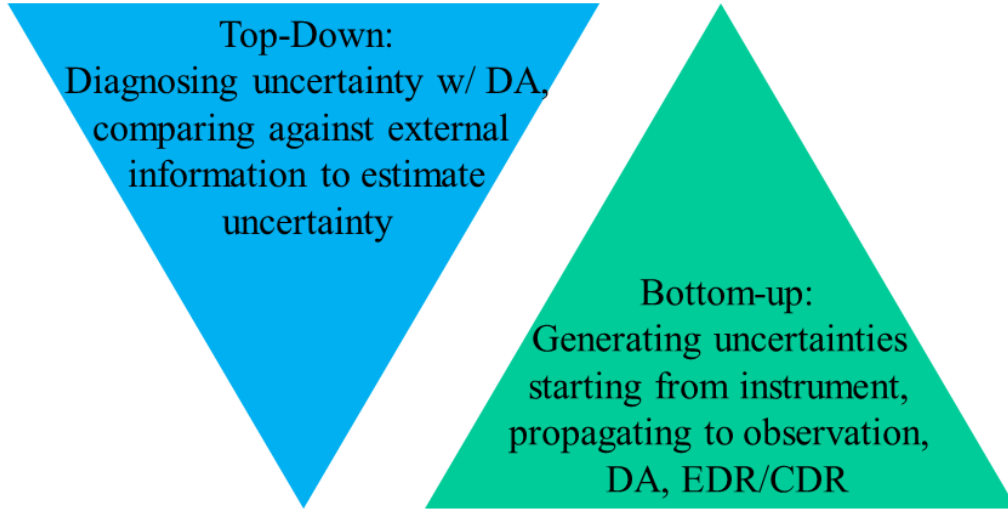


Figure 2: Comparison of the top-down and bottom-up approaches for observation uncertainty quantification. The error inventory ERRSat is a bottom-up approach.

can weigh different observations and models for developing high-quality EDR/CDR. Also, satellite measurement error can arise from a range of sources, and error identification and quantification improve hardware development.

There are basically two ways for uncertainty quantification, the top-down and bottom-up approaches (Figure 1). Most of DA-base diagnostics fall into the first category, that is, starting from the satellite observations and then iteratively diagnosing the uncertainty. This approach is affected by observational data, diagnostic techniques. An error inventory is a bottom-up approach and can provide information of error propagation.

## 1.2 ERRSat Overview

The **Error Representation and Realization of Satellite** observation (ERRSat) is a satellite observation error inventory. ERRSat is a bottom-up approach, with error generating and forward propagation. ERRSat can simulate a variety of satellite observation errors. Individual or compound error sources can be turned on and off for applications under different scenarios. With the simulated error at the pixel level, ERRSat provides the uncertainties for assimilating satellite data. The uncertainty information is based on physical models that are a much more accurate representation than the fixed or empirical uncertainties.

Applications of ERRSat covers a broad areas such as:

- Simulating error and studying error propagation in assimilating satellite data
- Generating ground truth testbed for validating and improving diagnostics
- Simulating error for EDR/CDR products
- Examining ground instrument tests, in-orbit satellite errors
- Calibrating and intercalibrating satellite sensors

ERRSat is developed in MATLAB and Python. The primary codes are developed in MATLAB,

without the prerequisite of advanced toolboxes. The simulator is highly vectorized for fast computing such as RTM, orbit, and collocation. It considers the application in Linux-like environment, allowing for breaking down tasks and submitting multiple jobs with hundreds or thousands cores. The simulator package comprises mostly scripts and several demo data with a total size of 3 MB. The source code has over 30,000 lines of code with over 300 scripts. The code is open source and freely available.

## 2 Download and Installation

### 2.1 Download

The ERRSAt source code is released in a compressed tarball via the GitHub ftp site:

<https://github.com/jxyangrs/errsats>

Additional documents and literature are also made available on GitHub. Also note permission may be needed to access the GitHub link. Please contact Dr. John Yang via email [jxyang@umd.edu](mailto:jxyang@umd.edu).

### 2.2 Installation

ERRSAt can be run in Windows, Mac, Linux-like OS. It basically needs no installation but MATLAB and Python. For Matlab, a version of 2016b or later that supports implicit expand for arithmetic operation is recommended. A Python 3 is suggested.

After downloading ERRSAt, change the current directory to the rootpath ‘‘~/errsats’’. The main script is `errsats_main.m`.

a quick check is run the command line after launching MATLAB and A message will pop out if it went great.

Figure 3 outlines the structure of ERRSAt. The simulator comprises a set of modules with a comprehensive error inventory. Various observation errors can be generated. We brief the modules as follows, and more details can be found in the manual online (<https://github.com/jxyangrs/ERRSAt>).

### 2.3 Code Directory

ERRSAt scripts are organized in a directory structure that subsets scripts per functionality. It is kept as straightforward as possible. The main script is `errsats_main.m` under the rootpath of ‘‘~/errsats/’’.

There are three sub-directories under ‘‘~/errsats/’’:

- The /src directory contains all source code files in Fortran-95, C/C++, IDL, BASH and JAVA.
- The /data directory contains sample data including satellite data, land-ocean mask, and one ERA5 data.
- The /doc directory includes help documents.

The ‘‘src’’ directory is the most important with sources code sorted out in a number of sub directories:

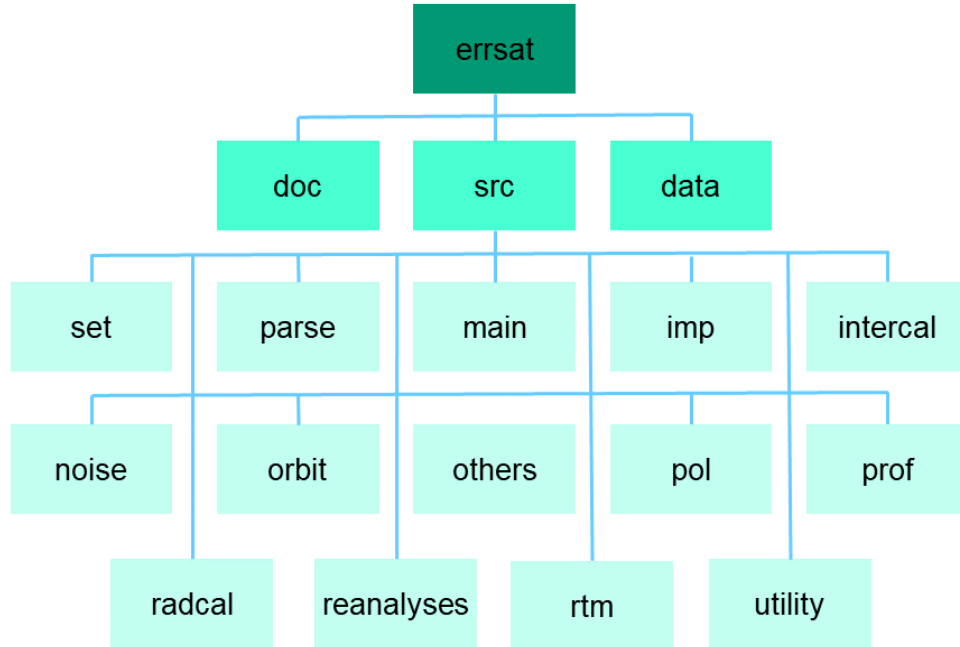


Figure 3: ERRSat code directory.

- The “/set” directory is for setting error sources, satellite, sensors, etc. Scripts in this directory are what users use most frequently.
- The “/parse” directory is parsing input and setting.
- The “/main” directory contains scenario scripts.
- The “/imp” directory includes scripts for function implementing such as error simulation.
- The “/intercal” directory is for single sensor or multiple sensor calibration and intercalibration.
- The “/noise” directory is for sensor noise simulation.
- The “/orbit” directory is for geolocation and pointing.
- The “/others” directory contains a third-party IGRF model.
- The “/pol” directory is about polarization computing.
- The “/prof” directory is for reading and processing data of profile like ERA5 and satellite data.
- The “/radcal” directory is for processing radiance into count, ta and tb.
- The “/reanalyses” directory is for downloading and processing ancillary reanalysis data.
- The “/rtm” directory include a RTM model.
- The “/utility” directory contains miscellaneous scripts such as data processing, visualization

Figure 3 depicts the directory structure.

## 2.4 Ancillary Input Files

ERRSat supports the use of ancillary data. These data are not included in ERRSat due to their large size, but we provide scripts for downloading, reading and writing. Reanalysis data such as ERA5, GDAS can be used for radiative transfer simulation. When Faraday rotation effect is considered, users can use electron profile, geomagnetic field. Various satellite data can be read in terms of geolocation, radiance. Users can also develop specific I/O scripts for specific satellite data.

## 2.5 Third Party Models

There are a variety of models that users can use and combine with ERRSat. We are aware of many well established models and do not seek to reinvent the wheel. We provide interface for input simulation results from third-party models.

For example, users can use other RTMs for simulating the TOA radiance and feed it to ERRSat. A number of RTM models include the Radiative Transfer for TOVS (RTTOV) and the Community Radiative Transfer Model (CRTM). Users can run their RTMs and feed the simulation results to our simulator.

Once errors are added into the radiance with ERRSat, there are lots of models, retrieval algorithms for processing radiance data into EDR/CDR products. For example, the NOAA’s Microwave Integrated Retrieval System (MIRS) is one of the powerful retrieval system based on 1-dimensional variational (1Dvar) inversion.

# 3 How to Use ERRSat

## 3.1 A Quick Start

Once you have obtained and installed ERRSat, you want to get familiar with it by running a few simple tests. A simple run is executing a series of steps with the first step of the command line:

```
errsat_main('step1')
```

Step-1 is running simulation from state vector to TOA radiance to count. The default setting can be found in the main script `errsat_main.m` as follows:

```
1 % -----  
2 % Input setting  
3 % -----  
4 % radiometer specification  
5 Setting.Rad.sensor = 'amsu-a'; % Demo_Oscillation/amus-a/mhs/amsr2/smap/atms/  
   Customize  
6 Setting.Rad.spacecraft = 'metop-a'; % optional for Demo_Oscillation; NOAA-19 for  
   AMSU-A/MHS; GCOM-W for AMSR2
```

where the sensor is `amsu-a` and spacecraft is `metop-a`.

The second step is converting count to  $T_A$ ,  $T_B$  by executing the command line:

```
errsat_main('step2')
```

You are done with the simple task. The results are in the newly created directory

“~/errsat/output/metop-a/amsu-a/simple”

where there are two sub-directory of “ /1sim” and “ /2cal”. The first sub-directory contains simulation of orbit, TOA  $T_B$ , count, etc. The second sub-directory is for calibrated  $T_A, T_B$  and plots.

## 3.2 Setting Error Sources

After finishing the simple task, let us move toward advanced settings. All of the settings are made in files in the directory “~/errsat/src/setting”. These settings can be found in the overall setting file `errsat_main_setting.m`, which is in the main script `errsat.m`

The content of the overall setting file `errsat_main_setting.m` is as follows

```
1 function errsat_main_setting
2 % overall setting of error sources, control configuration
3 %   A number of settings can be set in this script. Users can customize these
   settings for specific error sources and
4 % configuration
5 %
6 % Input:
7 %       setting a range of error sources, control configuration
8 %
9 % Output:
10 %      customized settings
11 %
12 % written by John Xun Yang, University of Maryland, jxyang@umd.edu, or
   johnxun@umich.edu, 10/03/2018: original code
13 % revised by John Xun Yang, University of Maryland, jxyang@umd.edu, or
   johnxun@umich.edu, 02/13/2020: review
14
15 global Setting Rad Noise Const Orbit TimeVarying TBsrc WarmLoad Reflector
   ScanBias PolOffset AP VarDynamic Prof Faraday Path
16
17 % =====
18 %% setting
19 % =====
20
21 % -----
22 % Input setting
23 % -----
24
25 % directory and scheme
26 errsat_set_path_scheme
27
28 % parsing input and preprocessing
29 errsat_parse_input
30
31 % -----
32 % radiometer basics
33 % -----
34
35 % radiometer basic specification
36 errsat_set_radspc
```



```

37
38 % radiometer channel specification
39 errsat_set_radspc_chan

```

where we only show the first 30 lines of the file. You can see a couple of settings, `errsat_set_path_scheme`, `errsat_set_radspc`, and `errsat_set_radspc_chan`. More details about the three settings can be found in the M-file. Overall, the file, `errsat_main_setting.m`, is where you can explore for specific settings.

Next, we take a look at an example about setting the receiver nonlinearity. The specific setting file is `errsat_set_nonlinear.m`. The content of the setting file is as follows:

```

1 function errsat_set_nonlinear
2 % setting receiver nonlinearity
3 %
4 % Input:
5 %     Rad.nonlinear.onoff,      turn on/off nonlinearity,          0/1
6 %     T_nl,                    peak nonlinearity of each channel (K), [1,
   channel]
7 %
8 % Output:
9 %     Rad.nonlinear.onoff,      turn on/off nonlinearity,          0/1
10 %    Rad.nonlinear.T_nl,       peak nonlinearity of each channel(K), [1,
   channel]
11 %
12 % Description:
13 %     The receiver nonlinearity is written as
14 %         Tas = Tc + X(Tw-Tc) + 4*T_nl*X*(1-X),                (1)
15 %     where Tas is the scene antenna temperature w/ nonlinearity (K), Tc is
   cold-space TB (K), Tw is warm-load TB (K), T_nl is the peak nonlinearity (K)
16 %     and X=(Cs-Cc)/(Cw-Cc) with Cs,Cc,Cw for scene count, cold count, and
   warm count respectively.
17 %     The first term, Tc + X(Tw-Tc), is the linear part, and 4*T_nl*X*(1-X) is
   the nonlinear part.
18 %     The maximum nonlinearity appears with X=0.5
19 %     Equation 1 is rewritten as
20 %         4*T_nl*X^2 - (Tw-Tc+4*T_nl)*X + Tas-Tc = 0
21 %         a*X^2+b*X+c = 0,                                     (2)
22 %     where a=4*T_nl, b=-(Tw-Tc+4*T_nl), c=Tas-Tc
23 %         X = 1/(2*a)*(-b-sqrt(b^2-4*a*c))
24 %     This is one of the two solutions, but a second solution is not physical
25 %         Cs = X*(Cw-Cc) + Cc,                                (3)
26 %     Tas often have more cross-track scans, and Tc,Tw,Cc,Cw have less scans
   and are averaged along cross-track and applied to Tas
27 %
28 % written by John Xun Yang, University of Maryland, jxyang@umd.edu, or
   johnxun@umich.edu, 01/31/2019: original code
29
30 global Rad
31
32 % -----
33 % setting
34 % -----
35 Rad.nonlinear.onoff = 0; % 0=off,1=on
36
37 if Rad.nonlinear.onoff ==1

```

```

38
39 % -----
40 % setting
41 % channel-dependent peak nonlinearity TB, [1,channel]
42 % -----
43 T_nl = 5*ones(1,Rad.num_chan);
44
45
46 % -----
47 % parse
48 % -----
49 errsats_parse_nonlinear
50
51 end

```

To turn on the reflector nonlinearity, you first set `Rad.nonlinear.onoff = 1` as in line 35. Then, set the magnitude of nonlinearity in line 43. This parameter is channel dependent. Details about the nonlinearity definition and calculation are given at the header of the script. The script `errsats_parse_nonlinear` in line 49 is for parsing the input and assuring the input parameters such as variable dimensions are correct.

### 3.3 Setting Modes

A comprehensive error inventory can be set with turning on/off of individual and combination. There are a few most common modes users may want to work with.

- **The Nominal Mode.**  
This refers to scenario of in-orbit spacecraft working in the nominal mode. The sensor observes Earth, with spillover seeing the cosmic background. In this mode, a couple of modules are turned on, including the orbit module, RTM, etc.
- **The Maneuver Mode**  
This mode is similar to nominal mode, but the spacecraft is flipped with the sensor looking at the cosmic background, with spillover pointing to Earth. This can be made by setting the targets of mainlobe, sidelobe and spillover.
- **The TVAC Mode**  
This is for ground Thermal Vacuum Chamber (TVAC) test. The scene target can be set to a uniform scene, with the RTM module turned off.

Table 1: The observation error inventory in the simulator

Setting	Nominal	Maneuver	TVAC
Orbit (errsats_orbit.m)	On	On	Off
RTM (errsats_set_geoorbit.m)	On	On	Off
Scene Target (errsats_set_modefarfieldTB.m)	On (Earth)	On (Cosmic)	On (Uniform Scene)

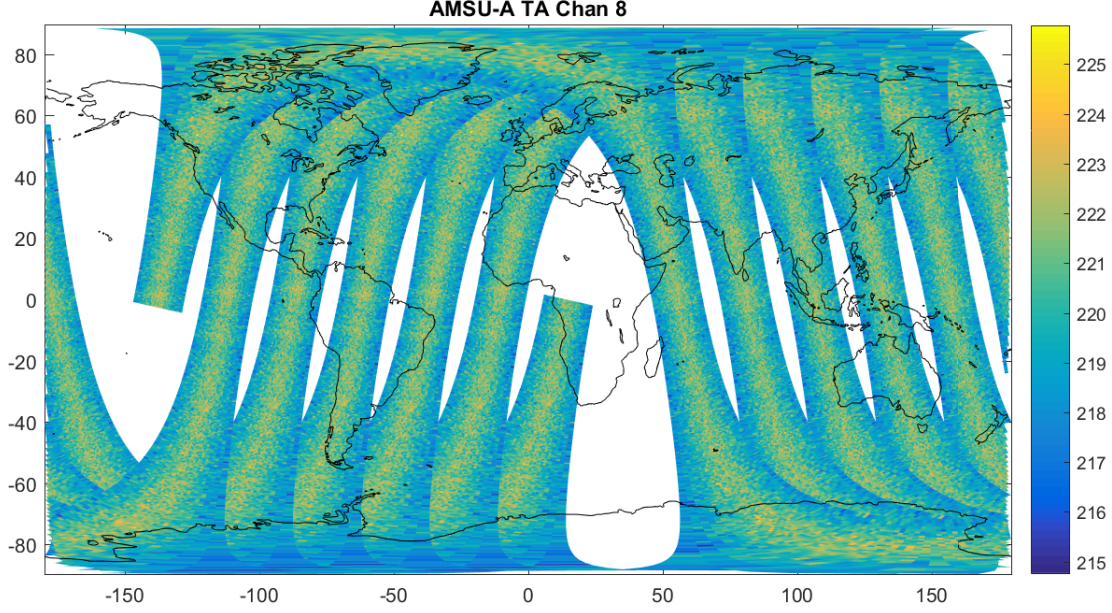


Figure 4: The Metop-A AMSU-A  $T_A$  of channel 8, with the simulated orbit and scanning. The atmospheric profile is the Standard U.S. Atmosphere, and thus there is no spatial variation. But ancillary data such as ERA5, GDAS can be used for more realistic simulation.

### 3.4 Output and Visualization

The output can have a range of files encompassing data and figures. The output is also dependent on what the setting and running mode is. The standard output data include the TOA  $T_B$ , counts, calibrated  $T_A$  and  $T_B$ , noise, etc. A number of figures are generated for visualization.

### 3.5 Advanced Setting

After getting familiar with the simulator, users can try more advanced setting. Among them include one category of combining a number of error sources. The comprehensive error inventory can be explored. For setting most of error source, go to `errsat_main_setting.m`. Note that there is dependency for setting some error sources. For example, the attitude offset (`errsat_set_attitudeoffset.m`) has dependency for satellite orbit setting (`errsat_set_georbit.m`). The dependency requirement is straightforward to find. In the afore-said case, it is described in the `errsat_set_attitudeoffset.m`.

ERRSat can be used for extensive simulation such as for processing one-year satellite data with ancillary reanalysis data. Given a Linux OS with a number of computing nodes and cores, users can break down the computing into many sub-task. For example, the one-year data can be subset to different date ranges, with one core for dealing with a specific time range. The code can also be set to break down a large orbital data (of a hundred minutes) into many granule data (of a couple of minutes) to fasten computing with multiple cores. We provide scripts for generating batch job submitting scripts such as in accordance with qsub, allowing for running hundreds of jobs at the same time.

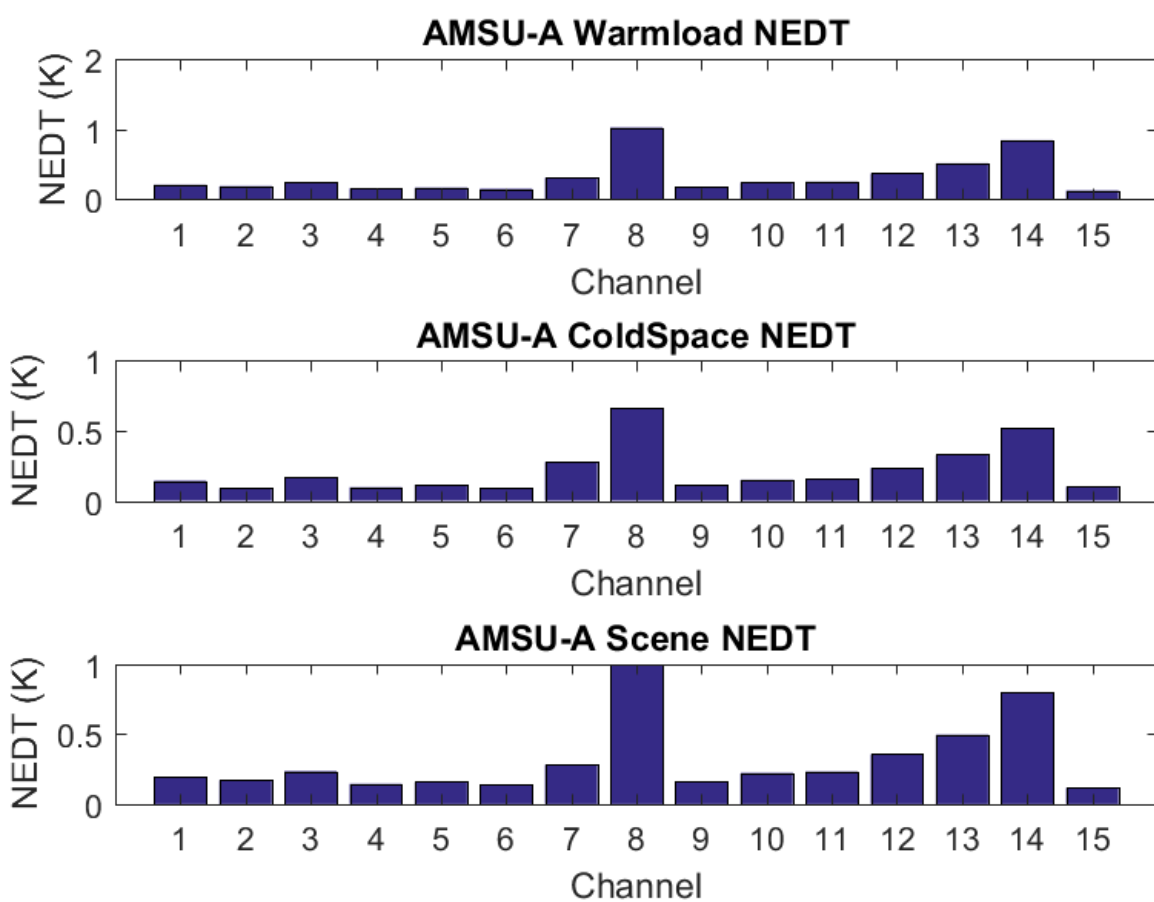


Figure 5: NEDT of Metop-A AMSU-A.

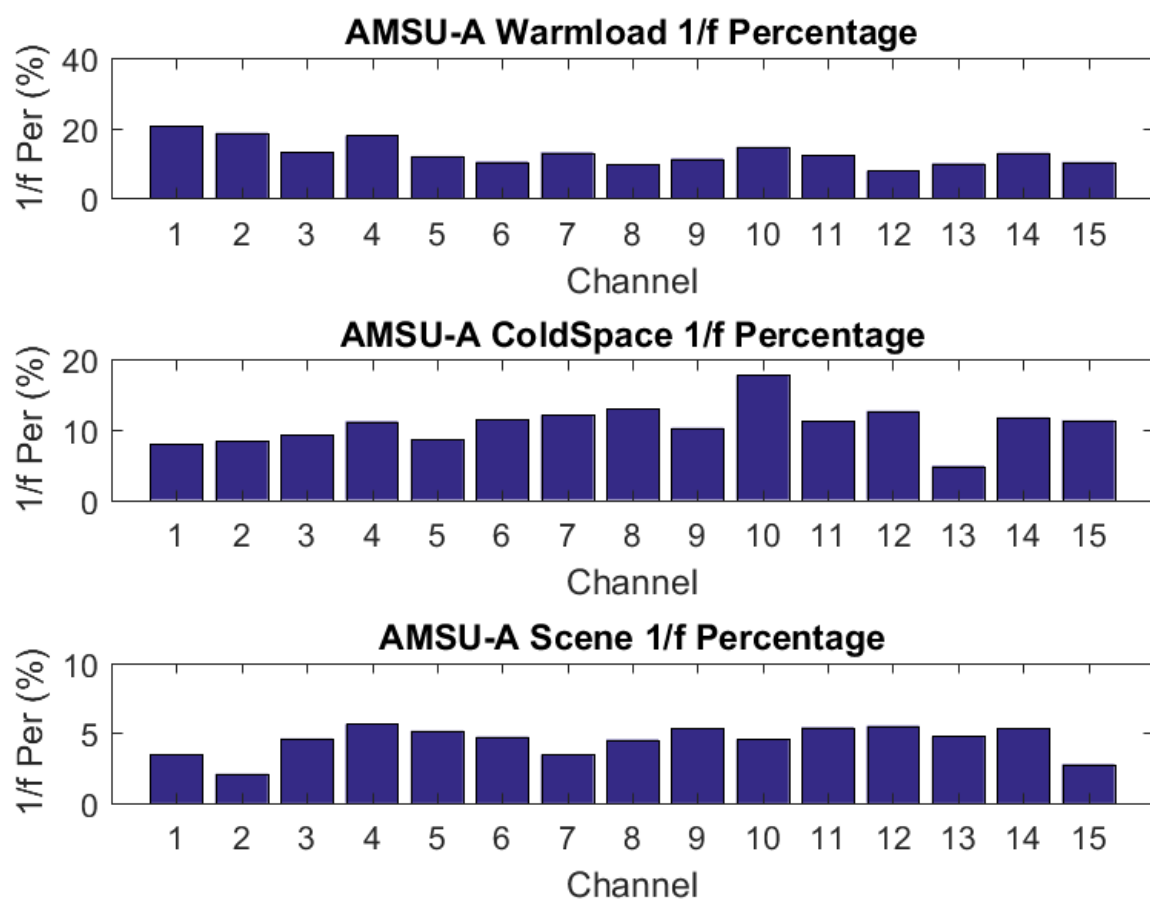


Figure 6: 1/f noise percentage.

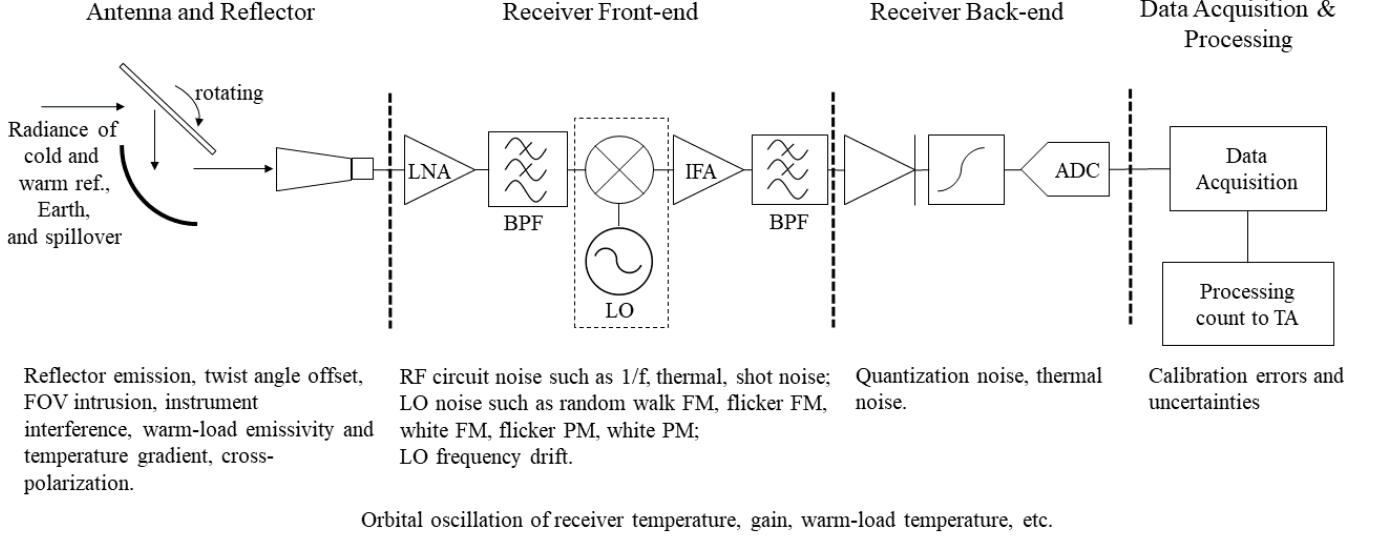


Figure 7: Diagram of a radiometer with noise and error sources illustrated.

## 4 Observation Error Inventory

### 4.1 Algorithm Basis

### 4.2 Measurement error

#### 4.2.1 Radiometer diagram

A radiometer comprises four parts. The reflector and antenna collect incoming radiance that enters the feedhorn followed by diplexers or orthomode transducers (OMT) for different channels. When the radiometer operates in the nominal mode, the radiance alternates between the cold-space, warm load, and Earth scenes, as the reflector spins. A ranges of errors can take place in this part as in the diagram and we will detail them shortly.

The receiver front-end is a key part. It comprises a cascade of a low-noise amplifier (LNA), LO if needed, and band-pass filters (BPF) where the incoming radiance gets amplified and filtered. During the process, electronic noise and other factors can affect the radiometer performance.

The receiver back-end is the video amplifying and recording. It has a square-law detector, video amplifier, and analog to digital converter (ADC). After data downlinking, the raw data are processed into level-1  $T_A$  and  $T_b$  as well as other science data in the ground data center.

#### 4.2.2 Generating count and $T_A$ with noise and orbital oscillation

The receiver processes radiance to count. After calibration, the count is converted to  $T_A$ . Noise from RF circuit is accompanied with the process. We developed a receiver module for processing count to  $T_A$  with generated noise.

The noise-free count of a radiometer can be written as *Ulaby et al.* [2014]

$$C = (T_A + T_R)G \quad (1)$$

where  $C$ ,  $T_A$  is antenna temperature,  $T_R$  is receiver temperature,  $G$  is the power gain. The system temperature can be defined as  $T_{sys} = T_A + T_R$ . In the presence of noise, it can be written as

$$C = (T_A + T_R + \sum n_i)G \quad (2)$$

where  $n_i$  represents a number of aforementioned individual noise, including both additive and signal-dependent noise. The short-term gain fluctuation also results in noise and can be counted as an individual  $n_i$  implicitly. The long-term gain oscillation subject to orbital variation is different from short-term fluctuation. It will be introduced in Section of Orbital Oscillation.

The noise term  $n_i$  and its generating can be associated with two families of additive and signal-dependent noise. The additive noise is written as ?

$$x = s + n \quad (3)$$

where  $x$  is the measurand,  $s$  is the signal,  $n$  is the additive noise that is signal independent. The additive noise model has mathematical advantages: noise can be generated with many random number generators, and the magnitude can be easily adjusted. The noise magnitude can be set and adjusted with respect to the channel-dependent NEDT *Ulaby et al.* [2014].

Thermal noise is due to the random motion of agitated charge carriers *Lee* [2004]; *Vasilescu* [2005]; *Schiek et al.* [2006]. The additive model is used to generate thermal noise. Thermal noise is treated as additive white Gaussian noise (AWGN) and generated with a pseudo random number generator (RNG). The default RNG is the Mersenne Twister and AWGN is assumed to be zero-mean *Matsumoto and Nishimura* [1998]. The noise generating is different in different runs. But in some cases, the same noise needs to be generated for testing the sensitivity of other error sources. This can be realized by fixing the RNG and its seed.

1/f noise is also called flicker noise or excess noise. It can arise from different mechanisms. It is found pronounced in electronics sensitive to surface phenomenon related to charge trapping and releasing and carrier generation and recombination *Lee* [2004]; *Vasilescu* [2005]; *Schiek et al.* [2006]. 1/f noise is produced with Fast Fourier Transform (FFT) *Sullivan et al.* [1990]; *Riley* [2008]. We first generate AWGN in the time domain. FFT transform is applied and multiplied with a term of power-law exponent of -1. The inverse FFT is applied for random numbers back in the time domain

$$\begin{aligned} h(\omega) &= \mathcal{F}(n_{\text{AWGN}}(t)) \\ n(t) &= \mathcal{F}^{-1}(h(\omega)f^\alpha) \end{aligned} \quad (4)$$

where the first equation denotes the Fourier transform of  $n_{\text{AWGN}}(t)$ , and the second one is the inverse transform with an additional power law term  $h(\omega)f^\alpha$ . For 1/f noise,  $\alpha = -1$ .

Phase and amplitude noise arise with a LO. This is very common for V/W/G bands, as LO performs heterodyning. A category of power-law noise can be produced, including the random walk FM noise ( $\alpha = -4$ ) related to oscillator environment, flicker FM ( $\alpha = -3$ ) from resonance mechanism, white FM ( $\alpha = -2$ ) from resonator frequency standards, flicker PM ( $\alpha = -1$ ) due to noisy electronics, white PM ( $\alpha = 0$ ) from phase noise in stages of amplification *Sullivan et al.* [1990]. The causes of noise are complex in practice and can come from multiple mechanisms. Oscillator noise is generated the same way with the FFT method.

Quantization noise is from ADC with  $\alpha = 2$  *Sullivan et al.* [1990]; *Schiek et al.* [2006]. It is also generated with the FFT method. Other power-law noise can also be generated in the simulator based on FFT transform with positive  $\alpha$  *Riley* [2008].

The signal-dependent noise is produced in a different way. Shot noise is due to the discrete nature of charger, and it is Poisson noise that depends on the signal *Lee* [2004]. It is generated with a Poisson RNG as *Kuan et al.* [1985]

$$n_{shot} = P_{\lambda}(T_{sys}) \quad (5)$$

where shot noise is a function of  $T_{sys}$  and  $P_{\lambda}$  is the Poisson RNG with  $\lambda$  as the Poisson distribution parameter.

The payload environment usually has an orbital oscillation as the spacecraft orbits the Earth ??????. It is due to the change of solar incidence angle and environment temperature along the orbit. The radiometer gain and warm-load temperature oscillate with a period same as the spacecraft orbital period ?. For MHS, the orbital period is  $\sim 100$  minutes. The orbital oscillation can be described as

$$\begin{aligned} T_W &= T_{W0} + \Delta T_W(t, \lambda, a, \phi) \\ G &= G_0 + \Delta G(t, \lambda, a, \phi) \end{aligned} \quad (6)$$

where  $T_{W0}$  and  $G_0$  are constant, and  $\Delta T_W$  and  $\Delta G$  are oscillation in terms of waveform as a function of time  $t$ , wavelength  $\lambda$ , amplitude  $a$ , and phase  $\phi$ . A variety of waveforms can be simulated. We can also import empirical orbital oscillations from observations as the oscillation term. In this study, we use sinusoidal wave with the empirical magnitudes from observation ?.

A radiometer observes both the cold and warm reference targets and the Earth scene during one complete rotation of the reflector. We generate counts as follows

$$\begin{aligned} C_W &= (T_{A,W} + T_R + n_W)G \\ C_C &= (T_{A,C} + T_R + n_C)G \\ C_S &= (T_{A,S} + T_R + n_S)G \end{aligned} \quad (7)$$

where  $T_{A,W}$ ,  $T_{A,C}$ , and  $T_{A,S}$  are the warm-load, cold-space, and Earth scene temperature, respectively.  $n_W$ ,  $n_C$ , and  $n_S$  are corresponding noise, and  $C_C$ ,  $C_W$ ,  $C_S$  are counts. If the warm-load is a perfect blackbody, there is  $T_{A,W} = T_W$ . And  $T_{A,C}$  equals the cosmic temperature  $T_C$ , if the cold-space view has no contamination from the reflector emission or field of view (FOV) intrusion.

The scanning mechanism of a radiometer determines the way of data sampling that should be counted in simulation. Figure 5 shows the diagram of MHS scan. As the reflector spins, the radiance received by the receiver alternates between the cold space, warm load, and Earth views. In between the effective objects, the radiometer is still working but sees the radiometer itself and the data are not usable. MHS has a rotation period of 2.67 seconds with a duty cycle of 68% for viewing Earth and reference targets *Robel and Graumann* [2014].

The scanning produces data as a conditional sampling with only a portion of data used. The recorded data are discrete chunks with gaps in between, and so is the noise. The conditional sampling has a profound influence. For instance, 1/f noise has a non-stationary mean that changes with time. The 68% duty cycle means longer time ( $1/0.68$ ) and larger variability for the same amount of data with 1/f noise compared to that without gaps. In addition, the discrete data with gaps can result in a difference between population statistics and sample statistics. Our simulator counts the scanning and sampling.

We simulate the null count of the other 35% measuring time as

$$C_N = (T_{A,N} + T_R + n_N)G \quad (8)$$



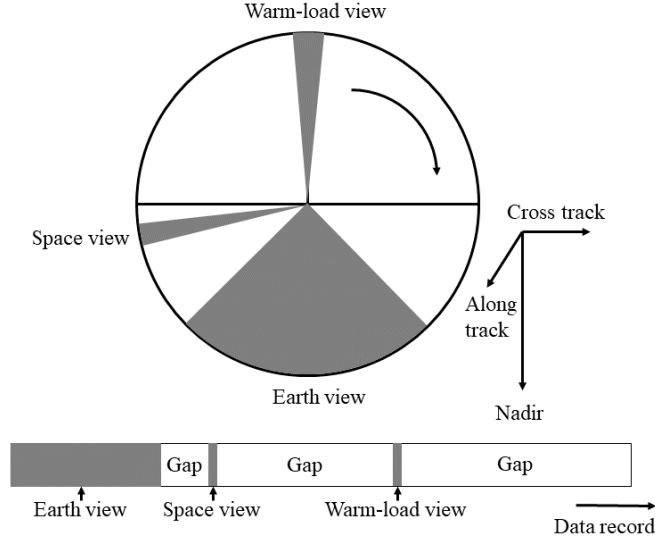


Figure 8: The scanning mechanism of MHS. In the nominal operating, the receiver sees the Earth, cold space, and warm load in turn with gaps in between as the reflector rotates. The duty cycle of the effective target views is about 68%. The data records are discrete chunks in time series, which is a conditional sampling. The data streaming is counted in the simulator.

where  $C_N$ ,  $T_{A,N}$ , and  $n_N$  denote the null count, scene temperature, and noise, respectively. The null simulation is not used but better represents MHS work mode of a conditional sampling.

After generating count for scene, cold and warm references,  $T_A$  is calculated

$$T_{a,s} = \frac{(T_w - T_c)}{(C_w - C_c)}(C_s - C_c) + T_c \quad (9)$$

where  $T_{a,s}$  is the scene temperature,  $T_w$  for warm load temperature,  $T_c$  is cold space temperature.  $C_w$ ,  $C_c$ ,  $C_s$  are count for warm load, cold space, and scene respectively.

If nonlinearity is considered, there is ATB [2016]

$$T'_{a,s} = T_{a,s} + 4T_n \frac{(C_s - C_c)}{(C_w - C_c)} \left[ 1 - \frac{(C_s - C_c)}{(C_w - C_c)} \right] \quad (10)$$

where  $T'_{a,s}$  is after nonlinear correction,  $T_{a,s}$  is from linear calibration,  $T_n$  is the term of peak nonlinearity that is often a look-up table from prelaunch test.

Examples of generated noise are shown in Figure 3. It is seen that noise can exhibit different characteristics in the time and frequency domain. For noise like 1/f noise, a distinct feature is that its mean is non-stationary with time. The same is true for its variance. This is different from thermal noise, which has a stationary mean and variance that is time invariant. These different noise can be set in a flexible way. Their magnitudes can be adjusted to the channel NEDT. They can be combined and blended with varying percentages. This is very useful to diagnose their characteristics and differentiate them.

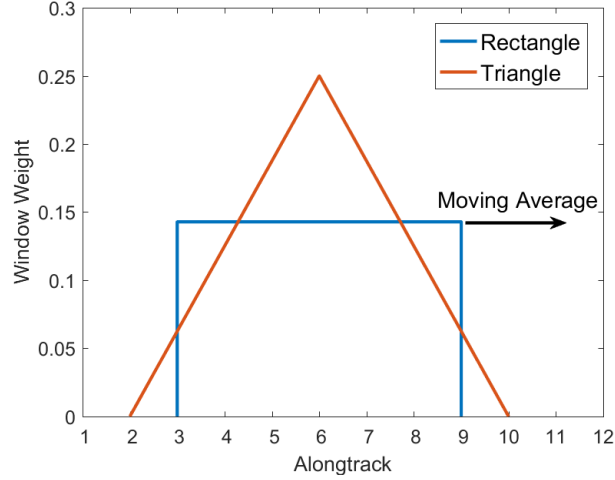


Figure 9: Examples of rectangular and triangular windows. The windows span a finite along-track length and are used for smoothing radiometer counts in deriving gain and brightness temperature.

#### 4.2.3 Windowing, calibration

This section present details of windowing and calibration. Windowing is used for smoothing cold-space and warm-load counts. The colds-space counts are smoothed as

$$\overline{C_{Cj}} = \frac{1}{n_{cc}} \sum_{k=j-n_1}^{j+n_2} w_k \sum_{i=1}^{n_{cc}} C_{Ci,j}, \quad (11)$$

where  $C_{Ci,j}$  is the cold-space counts as a function of scan positions in terms of cross-track  $i$  and along-track  $j$ . We refer cross-track measurements as *samples* and along-track measurements as *scans* hereafter.  $n_{cc}$  is the number of cross-track samples of cold counts. For exmaple, ATMS and MHS have  $n_{cc} = 4$ .  $n_1$  and  $n_2$  are related to the window length  $L$  through the floor function as

$$n_1 = \lfloor \frac{L-1}{2} \rfloor \quad \text{and} \quad n_2 = \lfloor \frac{L}{2} \rfloor. \quad (12)$$

$w_k$  is a window function with a length of  $L$  for smoothing counts along track.  $w_k$  can be a rectangular window as

$$w_k = \frac{1}{L}, \quad 0 \leq k \leq L-1. \quad (13)$$

A triangular window is also often used as

$$w_k = \begin{cases} \frac{2}{L+1} \left(1 - \frac{|2k-L+1|}{L+1}\right), & 0 \leq k \leq L-1, \text{ odd } L, \\ \frac{2}{L} \left(1 - \frac{|2k-L+1|}{L}\right), & 0 \leq k \leq L-1, \text{ even } L. \end{cases} \quad (14)$$

A triangular window of  $L = 7$  has been used for all MHS and AMSU-A/B at EUMETSAT and NOAA *Mo* [1996]; *Weng et al.* [2013]; [?]; [?]; *Robel and Graumann* [2014].

Likewise,  $C_{Wi,j}$  is smoothed

$$\overline{C_{Wj}} = \frac{1}{n_{cw}} \sum_{k=j-n_1}^{j+n_2} w_k \sum_{i=1}^{n_{cw}} C_{Wi,j}, \quad (15)$$

where  $n_{cw}$  is the cross-track number of warm-load counts.

The warm-load PRT temperature, from the average of multiple PRTs, is smoothed as

$$\overline{T_{Wj}} = \sum_{k=j-n_1}^{j+n_2} w_k T_{Wj}. \quad (16)$$

Then, the power gain  $\overline{G_{Sj}}$  is given by

$$\overline{G_j} = \frac{\overline{C_{Wj}} - \overline{C_{Cj}}}{\overline{T_{Wj}} - T_C}, \quad (17)$$

where  $T_C$  is the cosmic temperature.

Earth scene antenna temperature is

$$T_{A,S_{i,j}} = \frac{1}{\overline{G_j}} (C_{S_{i,j}} - \overline{C_{Cj}}) + T_C, \quad 1 \leq i \leq n_{cs}. \quad (18)$$

where  $n_{cs}$  is the cross-track number of Earth scene.

In addition to Earth scene, it is useful to derive warm-load and cold-space antenna temperature for determining the Noise Equivalent Delta Temperature (NEDT) and decomposing noise. In contrast to the cold-space counts, we split the cross-track warm-load counts into two subsets for deriving the gain and warm-load antenna temperature  $T_{A,W}$ . Doing so assures the independency between the derived gain and  $T_{A,W}$ , avoiding generating a pseudo  $f^2$  in the frequency domain due to the inappropriate signal processing ?. A pseudo  $f^2$  noise spectrum underestimates 1/f noise since its low-frequency regime is ignored ?. We suggest reader refer to ? for details.

We first smooth half of cross-track  $C_{W_{i,j}}$  as

$$\overline{C_{W_{i,j}}} = \frac{2}{n_{cw}} \sum_{k=j-n_1}^{j+n_2} w_k \sum_{i=1}^{\frac{n_{cw}}{2}} C_{W_{i,j}}, \quad 1 \leq i \leq \frac{n_{cw}}{2}, \quad (19)$$

where  $n_{cw}$  is number of cross-track warm counts, which is four for MHS. Then, the power gain  $\overline{G_{CWj}}$  is given by

$$\overline{G_{CWj}} = \frac{\overline{C_{W_{i,j}}} - \overline{C_{Cj}}}{\overline{T_{Wj}} - T_C}, \quad 1 \leq i \leq \frac{n_{cw}}{2}, \quad (20)$$

where  $T_C$  is the cosmic temperature.

The other half of cross-track  $C_{W_{i,j}}$  is used for deriving the warm-load antenna temperature  $T_{A,W}$

$$T_{A,W_{i,j}} = \frac{1}{\overline{G_{CWj}}} (C_{W_{i,j}} - \overline{C_{Cj}}) + T_C, \quad \frac{n_{cw}}{2} + 1 \leq i \leq n_{cw}. \quad (21)$$

#### 4.2.4 Decomposing Noise

In the above section, we obtain the cold-space or warm-load antenna temperature. We proceed to derive the noise. The orbital oscillations is removed with the warm-load PRT

$$\Delta T_{A,W_{i,j}} = T_{A,W_{i,j}} - \overline{T_{Wj}}, \quad \frac{n_{cw}}{2} + 1 \leq i \leq n_{cw}, \quad (22)$$

where  $\Delta T_{A,W}$  is the warm-load noise.

NEDT is the unbiased second central moment of noise ?

$$\text{NEDT}_{\text{total}} = \sqrt{\frac{1}{MN-1} \sum_{j=1}^N \sum_{i=1}^M (\Delta T_{A,W_{i,j}} - \overline{\Delta T_{A,W}})^2}, \quad (23)$$

where  $\Delta T_{A,W}$  is a  $M \times N$  matrix, and  $\overline{\Delta T_{A,W}}$  is

$$\overline{\Delta T_{A,W}} = \frac{1}{MN} \sum_{j=1}^N \sum_{i=1}^M \Delta T_{A,W_{i,j}}. \quad (24)$$

We can break down total noise into thermal and 1/f noise based on their spectra information, since thermal noise dominates on a small time scale while 1/f noise is significant on a large time scale ?. Thermal noise is calculated as ?

$$\text{NEDT}_{\text{thermal}} = \sqrt{\frac{1}{2N(M-1)} \sum_{j=1}^N \sum_{i=1}^{M-1} (\Delta T_{A,W_{i+1,j}} - \Delta T_{A,W_{i,j}})^2}. \quad (25)$$

The above equation calculates the unbiased standard deviation of adjacent cross-track samples of a time scale of a couple of milli-second. The above equation is based on Allan deviation, which is an unbiased estimate of thermal noise that is Gaussian additive white noise ??.

1/f noise is given by

$$\text{NEDT}_{1/f} = \sqrt{(\text{NEDT}_{\text{total}}^2 - \text{NEDT}_{\text{thermal}}^2)}. \quad (26)$$

In the presence of noise other than thermal and 1/f noise, this equation gives the magnitude of non-thermal noise.

The  $1/f$  percentage is defined as ?

$$P_{1/f} = \frac{\text{NEDT}_{1/f}^2}{\text{NEDT}_{\text{total}}^2} \times 100\%. \quad (27)$$

$P_{1/f}$  ranges from 0 to 100%. In ?, the partitioning of thermal and 1/f noise has been validated with simulation and observation. While we have calculated noise of warm-load, the similar procedure can be applied to derive the cold-space noise as well.

#### 4.2.5 Cross-pol Contamination

The antenna main polarization (co-pol) sees some radiation leakage from the orthogonal polarization plane (cross-pol). The cross-pol leakage can be due to the antenna asymmetry, defects, excitation of higher-order modes ?*Davis and Agarwal* [2011]; ?. Cross-pol correction is a necessary step in APC. In the simulator, the cross-pol is a  $4 \times 4$  matrix as

$$\begin{bmatrix} T'_v \\ T'_h \\ T'_3 \\ T'_4 \end{bmatrix} = \begin{bmatrix} C_{vv} & C_{vh} & C_{v3} & C_{v4} \\ C_{hv} & C_{hh} & C_{h3} & C_{h4} \\ C_{3v} & C_{3h} & C_{33} & C_{34} \\ C_{4v} & C_{4h} & C_{43} & C_{44} \end{bmatrix} \begin{bmatrix} T_v \\ T_h \\ T_3 \\ T_4 \end{bmatrix} \quad (28)$$

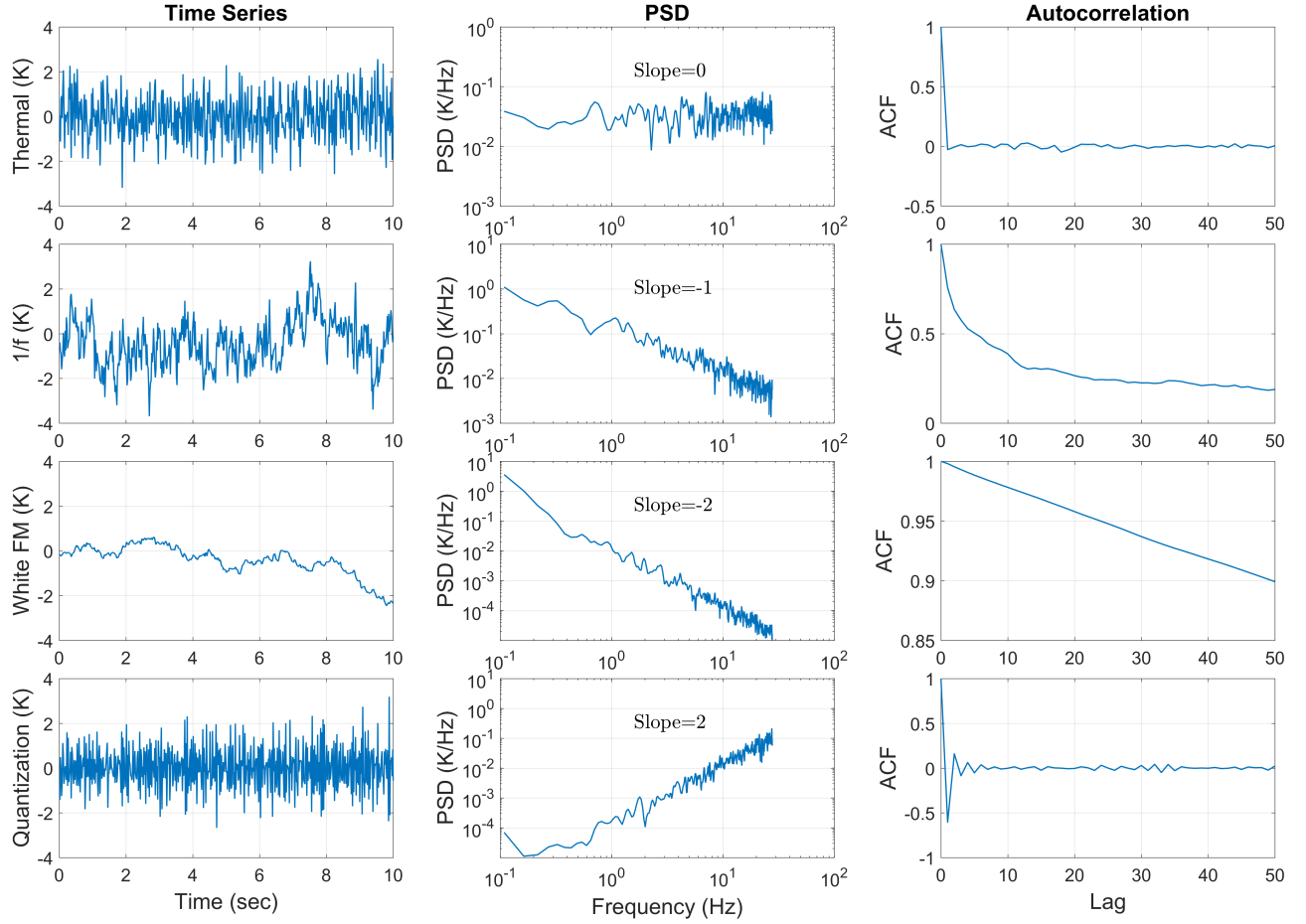


Figure 10: Examples of simulated noise in time series, power spectrum, and auto-correlation. These include thermal noise, 1/f, white FM, and quantization from up to down, which exhibit different characteristics in the time and frequency domain.

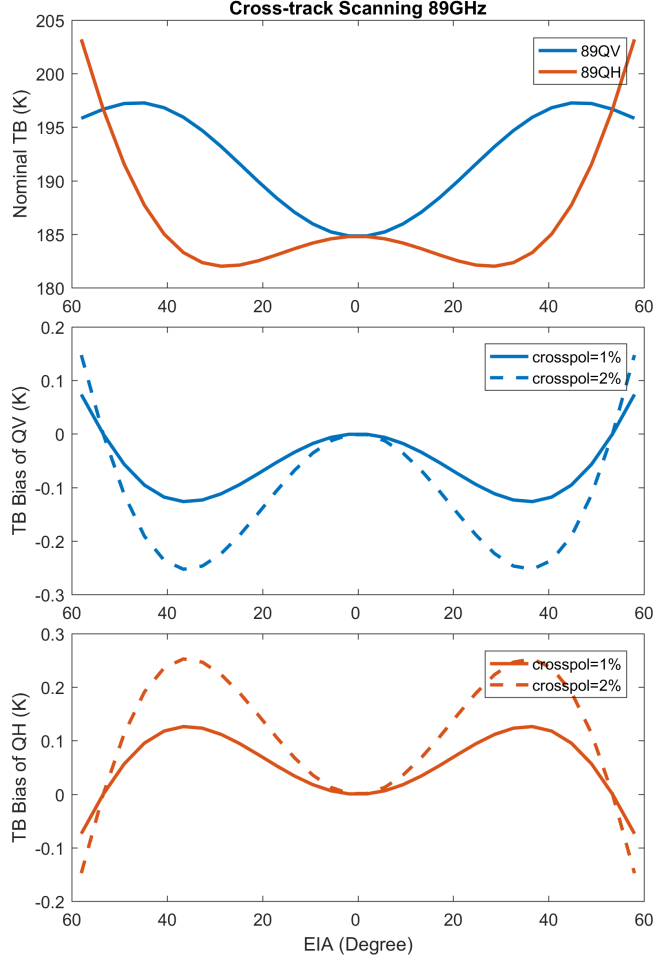


Figure 11: Effect of cross-pol leakage for cross-track scanning radiometers at 89 GHz of QV and QH. The panels show the (a) nominal TBs, (b) bias at QV, and (c) bias at QH. The RTM simulation assumes mid-latitude winter atmospheric profiles with a SST of 290 K and a wind speed of 5 m/s.

where the  $C_{i,j}$  is cross-pol coefficients that transforms the cross-pol free Stokes (right) to the new Stokes (left). The values of the coefficients can be customized. In the case of cross-pol free, the matrix is the identity matrix. Examples of cross-pol sensitivity are presented in the results.

#### 4.2.6 Twist angle offset

The twist angles refer to a set of reflector and polarization angles that affect radiance and polarization. For a cross-track scanning radiometer like AMSU-A and MHS the channel  $T_b$  is ??:

$$\begin{aligned} T_{b,qv} &= A^2 T_{b,v} + B^2 T_{b,h} \\ T_{b,qh} &= A^2 T_{b,h} + B^2 T_{b,v} \end{aligned} \quad (29)$$

where  $T_{b,qv}$  and  $T_{b,qh}$  are the quasi-V and quasi-H brightness temperature respectively, and  $T_{b,v}$  and  $T_{b,h}$  are  $T_b$  of the vertical polarization (v-pol) and horizontal (h-pol) respectively. Without any angular offset, there is  $A = \cos \phi$  and  $B = \sin \phi$  with  $\phi$  as the scan angle.

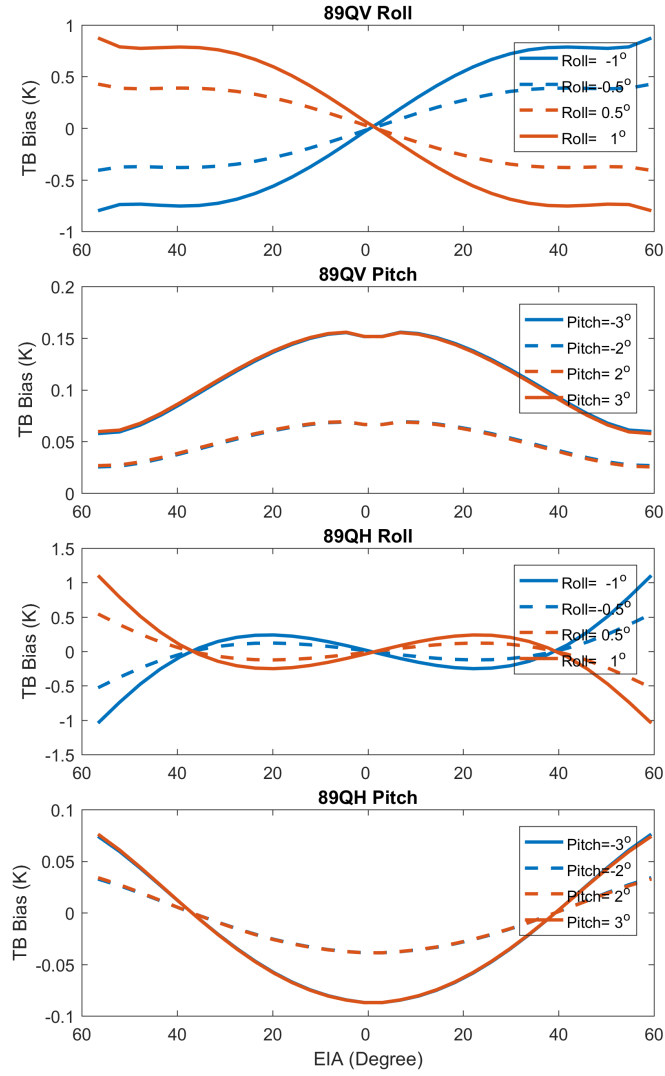


Figure 12: Attitude biases at 89 GHz QV and QH of cross-track scanning radiometers for (upper two panels) roll and (lower two panels) pitch.

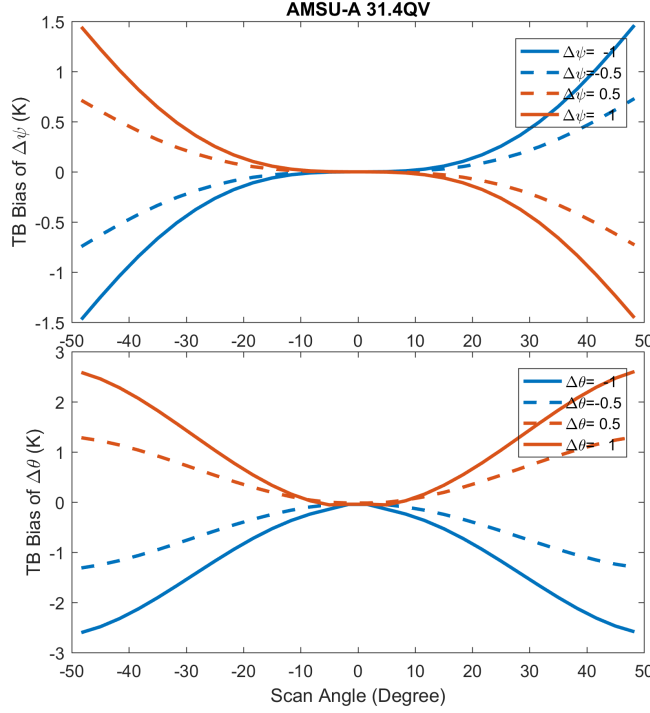


Figure 13: Sensitivity of twist angle offset for AMSU-A channel-2 of 31.4 GHz QV. a) The sensitivity of polarization alignment angle  $\psi$  and b) the sensitivity of reflector angle  $\theta$ .

The equation can be rewritten as a function of twist angles as

$$A = \frac{1}{\sqrt{1 - \sin^2 2\theta \cos^2 \phi}} \cdot [\cos 2\theta \sin \psi - 2 \sin \theta \cos(\phi + \psi) \sin \phi] \quad (30)$$

$$B = \frac{1}{\sqrt{1 - \sin^2 2\theta \cos^2 \phi}} \cdot \{ (\cos^2 2\theta + \sin^2 2\theta \sin^2 \phi) \cdot [2 \sin^2 \theta \cos(\phi + \psi) \cos \phi - \cos \psi] - \frac{1}{2} \sin^2 2\theta \sin 2\phi [2 \sin^2 \theta \cos(\phi + \psi) \sin \phi + \sin \psi] - \frac{1}{2} \sin 4\theta \cos \phi \sin 2\theta \cos(\phi + \psi) \} \quad (31)$$

where twist angles include  $\theta$  of the reflector angle,  $\psi$  of the polarization alignment angle, and  $\phi$  of the scan angle. The nominal reflector and polarization alignment angles without offset are  $\theta = 45^\circ$  and  $\psi = 90^\circ$ , and the above two equations reduce to  $A = \cos \phi$  and  $B = \sin \phi$ . The twist angles can be tuned to examine their impact on  $T_b$ . We present results in Section III.

Unlike cross-track scanning, a conical scanning radiometer has constant scan angles. We only consider the offset in the polarization alignment angle  $\psi$ , which is the same as in Equation 11.



#### 4.2.7 Spacecraft attitude and geolocation

A spacecraft and onboard sensor can have attitude errors in terms of roll, pitch, and yaw. The attitude changes the FOV geolocation and incidence angle and therefore the scene temperature *Meissner and Wentz* [2006]; *Kroodsmma et al.* [2012]. Attitude is also linked to other error sources such as Faraday rotation which is dependent on FOV geolocation and angles.

A module is developed for performing coordinate systems and transformation *Cai et al.* [2011]. The steps for coordinate transformation are briefed as follows. The error-free cross-track or conical scanning vector is computed in the local spacecraft frame of North-East-Down (NED) coordinate. The rotation matrix for the attitude is calculated and applied to the scan vector. The new scan NED vector is transformed to the Earth-centered Earth-fixed (ECEF) geocentric coordinate. The line-of-sight intersection on the ground is computed, and the FOV geolocation is determined. The geodetic coordinate, including FOV geolocation and azimuth and incidence angle, is obtained by transforming the FOV vector from geocentric to geodetic coordinate. The Earth ellipsoid model of WGS-84 is used, while a customized ellipsoid can also be used. The FOV geolocation and angles on the ionosphere shell are computed in the same way but with new ellipsoid parameters counting ionosphere altitude.

The afore-said transforms are from the radiometer to the Earth. It can also be inverted: the input can be realistic FOV geolocations and spacecraft orbit, and the scan NED vector can be determined. Then the attitude can be applied. By doing so, attitude is applied to any operating radiometers. In addition to observational data, the simulator also includes a Keplerian orbit model that simulates a spacecraft orbit *Griffin* [2004]. The orbit can be designed with the six orbit elements. This allows studying attitude in a more idealized but versatile way since the orbit and scan are flexible.

#### 4.2.8 Antenna pattern

Antenna pattern determines the weighted radiance a radiometer receives in all solid angles *Balanis* [2015]. APC is necessary in calibration to process weighted  $T_A$  to the scene  $T_b$ . Antenna pattern can be measured on the ground, and a hybrid one with both measurement and modeling is often used. Errors in the antenna pattern result in  $T_b$  bias when there is an overestimate or underestimate of sidelobe and spillover. And the bias is not a constant but dependent on the scene temperature since APC has a scaling effect.

A module is included in the simulator to study the antenna pattern impact. Antenna pattern can be parameterized for the mainlobe, sidelobe, and spillover. The fractions of them can be customized with respect to specific radiometers. Different FOV targets can be set for the mainlobe, sidelobe and spillover. For instance, the nominal operating can be set to have mainlobe and sidelobe viewing the ocean with the cosmic background for spillover. To simulate the deep-space maneuver when the radiometer is flipped upside down, the mainlobe and sidelobe can be set viewing the cosmic with the spillover toward the Earth.

#### 4.2.9 Faraday rotation

Faraday rotation takes place when a polarized EM wave goes through the ionosphere with the geomagnetic field *Meissner and Wentz* [2006]; *Peng et al.* [2017]. The E-field vector of the EM wave rotates and the Stokes vector is altered. Faraday rotation is dependent on the EM frequency, ionosphere electron content, and the geomagnetic field. It is pronounced at low-frequencies like L-band and for polarimetric radiometers like WindSat where the second and third Stokes are measured.

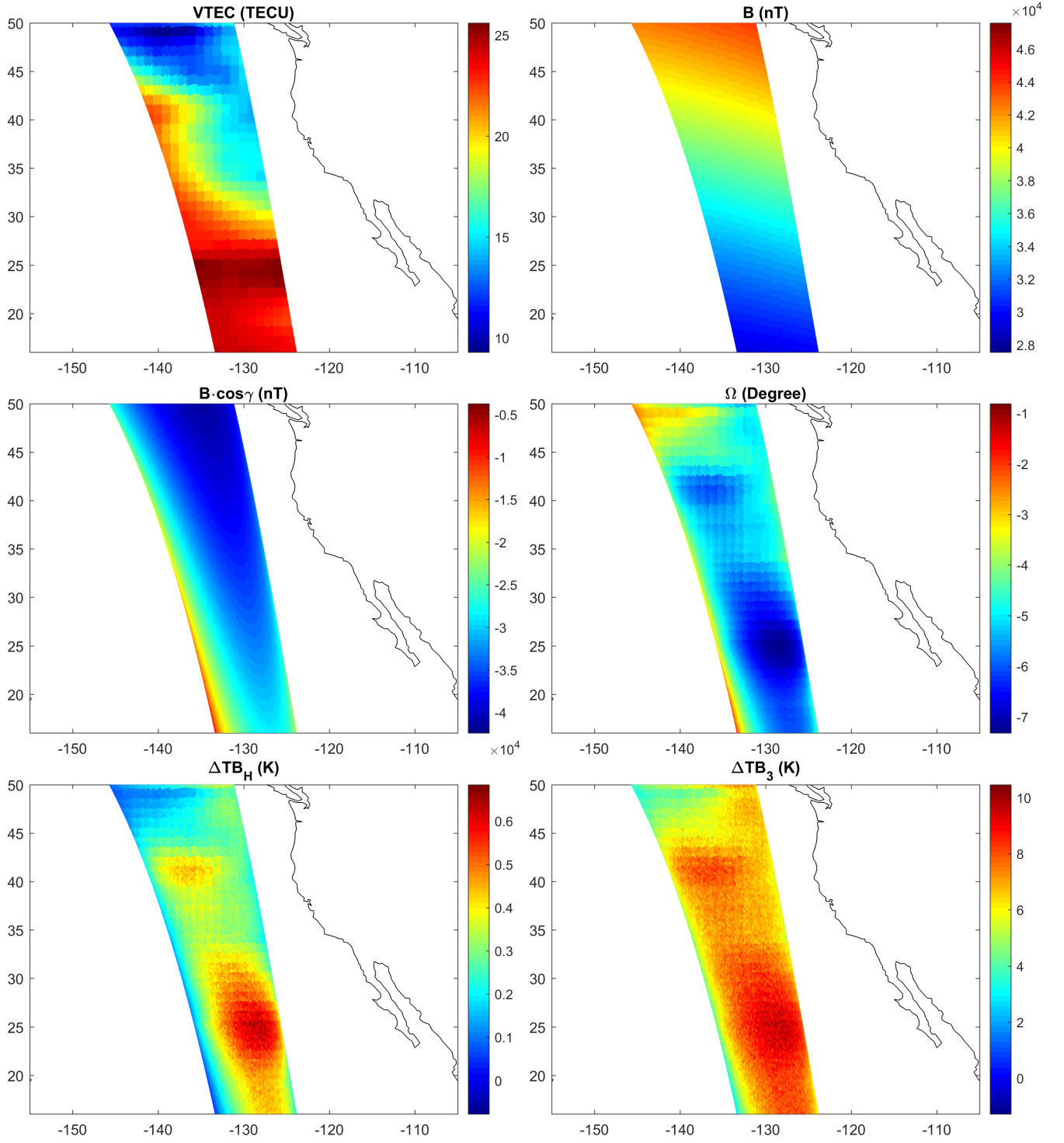


Figure 14: Channel correlation due to cross-talk. (a) Measured cross-talk of NPP ATMS. (b) simulated cross-talk for ATMS.

It can be written by *Meissner and Wentz* [2006]; *Peng et al.* [2017]

$$\Omega = \frac{2.365 \cdot 10^2}{f^2} \cdot B \cos \gamma \cdot \text{VTEC} \sec \theta \quad (32)$$

where  $\Omega$  is in radian,  $f$  is the frequency in GHz,  $B$  is the geomagnetic field in Tesla, and  $\gamma$  in radian is the angle between the EM wave and B field. VTEC is the integral of vertical total electron content in TEC unit (TECU), where 1 TECU is  $10^{16}$ electron/ $m^2$ . And  $\theta$  in radian is the angle between the EM wave and ionosphere.

Faraday rotation can be written in the modified Stokes

$$\begin{bmatrix} T'_v \\ T'_h \\ T'_3 \\ T'_4 \end{bmatrix} = \begin{bmatrix} \cos^2 \Omega & \sin^2 \Omega & 1/2 \sin 2\Omega & 0 \\ \sin^2 \Omega & \cos^2 \Omega & -1/2 \sin 2\Omega & 0 \\ -\sin 2\Omega & \sin 2\Omega & \cos 2\Omega & 0 \\ 0 & 0 & 0 & 1 \end{bmatrix} \begin{bmatrix} T_v \\ T_h \\ T_3 \\ T_4 \end{bmatrix} \quad (33)$$

where the right side Stokes is before entering ionosphere and the left side one is with Faraday rotation effect.

The simulator treats the electron content as a shell from the ground *Meissner and Wentz* [2006]; *Peng et al.* [2017]. The altitude of the shell is adjustable and the default setting is 400 km. The ionosphere altitude can also be varied to account for the fact it has a lower altitude toward the poles. The geolocation of EM waves on the ionosphere is calculated with the Earth mapping module provided the spacecraft orbit and scan geometry. The IGRF model is included as a module for computing the geomagnetic field *Thébault et al.* [2015]. The total electron content can be obtained from observations or models and imported to the simulator *Bilitza et al.* [2017].

#### 4.2.10 Cross-polarization leakage

The antenna main polarization (co-pol) sees some radiation leakage from the orthogonal polarization plane (cross-pol). The cross-pol leakage can be due to the antenna asymmetry, defects, excitation of higher-order modes *Ruf* [1998]; *Davis and Agarwal* [2011]; *Balanis* [2016]. Cross-pol correction is a necessary step in APC. In the simulator, the cross-pol is a  $4 \times 4$  matrix as

$$\begin{bmatrix} T'_v \\ T'_h \\ T'_3 \\ T'_4 \end{bmatrix} = \begin{bmatrix} C_{vv} & C_{vh} & C_{v3} & C_{v4} \\ C_{hv} & C_{hh} & C_{h3} & C_{h4} \\ C_{3v} & C_{3h} & C_{33} & C_{34} \\ C_{4v} & C_{4h} & C_{43} & C_{44} \end{bmatrix} \begin{bmatrix} T_v \\ T_h \\ T_3 \\ T_4 \end{bmatrix} \quad (34)$$

where the  $C_{i,j}$  is cross-pol coefficients that transforms the cross-pol free Stokes (right) to the new Stokes (left). The values of the coefficients can be customized. In the case of cross-pol free, the matrix is the identity matrix. Examples of cross-pol sensitivity are presented in the results.

#### 4.2.11 Reflector emission

An ideal reflector has no self-emission with emissivity equal to zero. In practice, its emissivity can be slightly larger than zero with self-emission seen by the receiver *Wentz et al.* [2001]; *Gopalan et al.* [2009]. The reflector emission introduces errors as it is mixed with radiance of Earth scene, cold and warm references. The emission can be negligible if the emissivity is small enough. An assessment of the reflector emissivity is always necessary.

A module in the simulator is for the reflector emission. It includes the setting for reflector emissivity and physical temperature. The reflector emissivity is dependent on frequency and polarization. For cross-track scanning, the emissivity is dependent on scan angle as it changes in different scan positions. It is insensitive to scan angle for a conical scanning radiometer as the scan angle is very constant. The reflector temperature is dependent on scan and orbit position.

#### 4.2.12 Cold-space mirror emission

For conical scanning radiometers, a cold-space mirror is often employed for the reflecting the cosmic background to the feedhorn. Its self-emission can lead to error in the cold reference. But the warmload and Earth scenes are unaffected, which is different from the reflector emission.

$$T_C = T_{\text{mirror}}\epsilon_{\text{mirror}} + T_C(1 - \epsilon_{\text{mirror}}) \quad (35)$$

where  $T_{\text{mirror}}$  is the mirror temperature,  $T_C$  is cosmic background,  $\epsilon_{\text{mirror}}$  is mirror emissivity.

#### 4.2.13 Warm load error

Warm load measurements can have errors. The onboard warm load is a blackbody. It is expected that it is a perfect blackbody with emissivity of one. This is opposite to the expectation of the reflector. The emissivity is less than one in practice *Twarog et al.* [2006]; ATB [2016]; *Alquaied et al.* [2018]. A correction is needed if the error is large enough. Additionally, the warm load error can come from the temperature gradient, which makes the PRT measured temperature deviate from the actual temperature. The situation can be pronounced when there is a solar intrusion on the warm load target, which induces a large temperature gradient *Twarog et al.* [2006]; ATB [2016]; *Alquaied et al.* [2018].

We provide a module for parameterizing the warm load error. The warm load effective temperature is a function of physical temperature, emissivity, and a bias term. The emissivity multiplied by the physical temperature is the apparent temperature. The emissivity ranges from zero to one. The bias term is a constant, and negative bias means the warm load temperature would be underestimated and positive bias means an overestimate of warm load temperature. The settings are channel dependent.

#### 4.2.14 FOV intrusion

FOV intrusion, or beam spoiling, occurs when the antenna FOV is obstructed by objects like the spacecraft or payloads. The effect has been found such as for SSM/I, TMI, AMSU-A *Colton and Poe* [1999]; *Wentz et al.* [2001]; *McKague et al.* [2010]. It is usually obvious at the edge of the scan. The intrusion errors can be parameterized by the temperature of the intrusion object and fraction of intrusion FOV *McKague et al.* [2010]

$$T_b = T_{b,\text{intr}}\Omega_{\text{intr}} + T_{b,\text{scene}}(1 - \Omega_{\text{intr}}) \quad (36)$$

where  $T_{b,\text{intr}}$  is the brightness temperature of the intrusion object,  $T_{b,\text{scene}}$  is for the Earth scene,  $\Omega_{\text{intr}}$  is the intrusion solid angle fraction.  $\Omega_{\text{intr}}$  is a function of scan position.  $\Omega_{\text{intr}}$  can be the error function assuming antenna pattern is a Gaussian function. And it can be further simplified as an exponential function when the FOV intrusion is small.  $T_{b,\text{intr}}$  can be set as a function of both cross-track and along-track scan.

#### 4.2.15 Bandpass spectral response

The spectral response is the bandpass responsivity of the finite bandwidth around the center frequency *Kim et al.* [2014]; ATB [2016]. The spectral response includes the response of amplifiers and BPFs and is dependent on the hardware. It usually exhibits channel-dependent responsivity that appears irregular than a flat spectrum. It is often measured in prelaunch tests. The effective channel radiance is the incoming radiance weighted by the spectral response.

The spectral response can be counted in the simulator. The channel bandpass can be split to plenty of sub-frequencies. A channel can have double sidebands or more subbands. RTM simulation is performed at every sub-frequency, and the channel effective brightness temperature is the convolution of  $T_b$  with the spectral response.

$$T_{b,chan} = \sum_{i=1}^n \int_{f_i-B_i/2}^{f_i+B_i/2} T_b(f) S_i(f) df \quad (37)$$

where  $T_{b,chan}$  is the channel effective brightness temperature,  $f$  is the sub-frequency,  $i$  is number of subband,  $f_i$  is the subband center frequency,  $B$  is the subband bandwidth,  $S_i(f)$  is the subband spectral response.

Doing so enables more accurate RTM simulations *Yang and Yang* [2018], since the atmospheric absorption is usually nonlinear in the finite bandpass. When the spectral response or atmospheric absorption nonlinearity is pronounced, a noticeable difference can be found between accurate simulation across the bandwidth and at only the center frequency of a channel.

#### 4.2.16 Interference of instrumental and geomagnetic field

Interference can take place due to the onboard instrument. For example, in the early flight phase of GMI, instrumental induced magnetic biases are found in all channels. The 10.65 GHz channel has a pronounced bias of 1.2 K of peak-to-peak. The bias is scan-dependent but is time invariant. The cause was later identified as instrumental interference of the reflector spin and feed switches on the launch restraints *Draper et al.* [2015]; *Wentz and Draper* [2016]. The variation of the geomagnetic field was also found to affect the radiometer. In our simulator, we consider the instrumental bias as an additive signal that is channel dependent. The additive bias can be customized and is added to  $T_A$ .

#### 4.2.17 Crosstalk

The inter-channel correlation can stem from crosstalk of hardware [*Ruf*, 1998; *Corbella et al.*, 2002; *Kim et al.*, 2014].

Crosstalk can be modeled in different ways. One simple way is

$$T_A = M \cdot T_A \gamma + T_A(1 - \gamma) \quad (38)$$

where  $M$  is the crosstalk matrix,  $\gamma$  is the reflection coefficient. The reflection can take place in the antenna sub-system.

#### 4.2.18 Count to antenna temperature

The count to  $T_A$  conversion is conducted with the two-point calibration. The cold-space counts are smoothed as

$$\overline{C_{Cj}} = \frac{1}{n_c} \sum_{k=j-n_1}^{j+n_2} w_k \sum_{i=1}^{n_c} C_{C_{i,j}}, \quad (39)$$

where  $C_{C_{i,j}}$  is the cold-space counts as a function of scan positions in terms of cross-track  $i$  and along-track  $j$ .  $n_c$  is the number of cross-track samples of cold counts.  $n_1$  and  $n_2$  are related to the window length  $L$  through the floor function as

$$n_1 = \lfloor \frac{L-1}{2} \rfloor \quad \text{and} \quad n_2 = \lfloor \frac{L}{2} \rfloor. \quad (40)$$

$w_k$  is a window function with a length of  $L$  for smoothing counts along track.  $w_k$  can be a rectangular window as

$$w_k = \frac{1}{L}, \quad 0 \leq k \leq L-1. \quad (41)$$

$w_k$  can also be a triangular window

$$w_k = \begin{cases} \frac{2}{L+1} (1 - \frac{|2k-L+1|}{L+1}), & 0 \leq k \leq L-1, \text{ odd } L, \\ \frac{2}{L} (1 - \frac{|2k-L+1|}{L}), & 0 \leq k \leq L-1, \text{ even } L. \end{cases} \quad (42)$$

A triangular window of  $L = 7$  has been used for all MHS and AMSU-A/B at EUMETSAT and NOAA ?*Robel and Graumann* [2014].

Likewise, the warmload counts are smoothed as

$$\overline{C_{Wj}} = \frac{1}{n_w} \sum_{k=j-n_1}^{j+n_2} w_k \sum_{i=1}^{n_c} C_{W_{i,j}}, \quad (43)$$

where  $C_W$  are the original warmload counts and  $n_w$  is the crosstrak number.

The warm-load PRT temperature, from the average of multiple PRTs, is smoothed as

$$\overline{T_{Wj}} = \sum_{k=j-n_1}^{j+n_2} w_k T_{Wj}. \quad (44)$$

The power gain  $\overline{G_j}$  is

$$\overline{G_j} = \frac{\overline{C_{Wj}} - \overline{C_{Cj}}}{\overline{T_{Wj}} - T_C}, \quad i = 1 \quad (45)$$

The Earth scene antenna temperature  $T_{A,E}$  is given by

$$T_{A,E_{i,j}} = \frac{1}{\overline{G_j}} (C_{E_{i,j}} - \overline{C_{Cj}}) + T_C, \quad 2 \leq i \leq 4 \quad (46)$$

where  $C_{E_{i,j}}$  is the Earth scene counts.

### 4.2.19 Antenna temperature to brightness temperature

The conversion of  $T_A$  to  $T_B$  is often referred to as the antenna pattern correction (APC). There are a number of steps in APC such as the correction for spillover, cross-pol contamination. Additional corrections are also needed in case of reflector emission, warmload error, FOV intrusion, etc. These corrections are included in the simulator, and can be turned on or off to study the sensitivity.

## 4.3 Observation operator error

### 4.3.1 Ancillary models and modules

A 1-D RTM is included in the simulator *Yang et al.* [2016]; *Yang and Yang* [2018]. The atmospheric gaseous absorption is based on the Rosenkranz model *Rosenkranz* [2017]; *Rosenkranz and Cimini* [2019]. An oceanic emission model is included ?. The users can also choose other surface and atmospheric absorption model and import the computed variables to the simulator.

The IGRF model is included for computing the geomagnetic field. It is the 12th generation of the model that covers from 1990 to the end of 2019 *Thébault et al.* [2015]. It is a series of models describing the geomagnetic field and is published by the International Association of Geomagnetism and Aeronomy (IAGA). The geomagnetic field is derived as the gradient of the magnetic scalar potential. The input for IGRF is geodetic coordinates, and the output is the vector of the geomagnetic field. Our simulator can also import and use geomagnetic fields produced by other models.

A Keplerian orbit model is used for simulating the spacecraft orbit *Griffin* [2004]. The input is the six orbit elements, and the output is the spacecraft geolocation. Orbital perturbations are not considered in the model, but it is sufficient to study effects like spacecraft attitude. Observational orbits can be imported to the simulator.

## 4.4 Representativeness error

Representativeness is due to the unresolved scales and processes, where the Numerical Weather Predicting (NWP) model resolution is usually coarser than satellite observations and has empirical parameterizations.

We develop a module for collocating satellite FOVs and the reanalyses, with the horizontal and vertical resolution adjustable. Accordingly, the RTM simulation can be conducted with a spatial resolution that the users define through the collocation. The resolution can be flexibly coarsened. A resolution finer than the reanalyses is realized by linear interpolation.

## 4.5 Pre-processing Error

The pre-processing is for screening data, such as rejecting observations that cannot be adequately modeled. Pre-processing can be involved with retrieval for converting radiance to state variables. Due to the limitation of filters and retrieval, pre-processing can give rise to error and uncertainties. We include a number of filters based on measured radiance for screening cloud, precipitation [].

The retrieval module includes several retrieval algorithms for processing radiance data into science products. It is for evaluating the impact of radiance errors on science products. For instance, empirical algorithms are included for retrieving atmospheric temperature, cloud liquid water content, oceanic surface wind speed [*Goodberlet et al.*, 1989; *Zhu and Weng*, 2013; *Rosenkranz*, 2006]. The retrieval can also be used for studying pre-screening in intercalibration.

Users can also refer to many established algorithms for producing EDR and CDR products, such as those at NOAA and EUMETSAT. For example, the NOAA’s Microwave Integrated Retrieval System (MIRS) is a comprehensive package based on 1D-variational (1DVar) inversion. MIRS can be used for studying error propagation in the retrieval.

## A Acronyms and Abbreviations

Acronyms	Description
ACF	Auto Correlation Function
ADC	Analog-To-Digit Converter
AGWN	Additive Gaussian White Noise
AMSU-A/B	Advanced Microwave Sounding Unit
APC	Antenna Pattern Correction
ATMS	Advanced Technology Microwave Sounder
BPF	Band Pass Filter
CDR	Climate Data Record
CLWP	Cloud Liquid Water Path
Cross-pol	Cross Polarization
CRTM	Community Radiative Transfer Model
EDR	Environmental Data Record
EM	Electromagnetic
ERA5	ECMWF Reanalysis V5
ERRSat	Error Representation and Realization of Satellite Observation
FM	Frequency Modulation
FOV	Field Of View
GDAS	Global Data Assimilation System
IGRF	International Geomagnetic Reference Field
LNA	Low Noise Amplifier
LO	Local Oscillator
MHS	Microwave Humidity Sounder
MIRS	Microwave Integrated Retrieval System
NEDT	Noise Equivalent Delta Temperature
NPP	National Polar-orbiting Partnership
O-A	Observation Minus Analysis
O-B	Observation Minus Background
OMT	Orthomode Transducer
PC	Principal Component
PCA	Principal Component Analysis
PM	Phase Modulation
PRT	Platinum Resistance Thermometers
PSD	Power Spectral Density
QH	Quasi Horizontal
QV	Quasi Vertical
RFIC	Radio Frequency Integrated Circuit
RNG	Random Nonise Generator
RTTOV	Radiative Transfer For TOVS
SVD	Singular Value Decomposition



T_A	Antenna Temperature
T_B	Brightness Temperature
TEC	Total Electron Content
TIROS	Television Infrared Observation Satellite
TOA	Top Of Atmosphere
TOVS	TIROS Operational Vertical Sounder
TVAC	Thermal Vacuum Chamber
VTEC	Vertical Total Electron Content

## B List of Error Sources

No.	Error Sources	Description
1	RFIC stationary noise	thermal noise, quantization noise in ADC, etc
2	RFIC non-stationary noise	1/f noise, shot noise, etc
3	local-oscillator noise	LO noise such as random walk FM, flicker FM, white FM, flicker PM
4	warm-load noise	noise in the warm load
5	gain jump	abrupt changes in the power gain
6	receiver nonlinearity	radiometric nonlinearity of the receiver
7	striping	radiometric stripes related to 1/f noise, thermal noise, and calibration
8	spectral response	bandpass spectral characteristics that are channel dependent
9	scanning and pointing	scanning angle error for viewing cold/warm reference, Earth scene
10	orbital oscillation	oscillation of warm load, receiver temperature, gain
11	twist angle offset	offsets in polarization alignment angle, reflector angle, scan angle
12	cross polarization	cross polarization leakage
13	cross talk	channel cross talk
14	reflector emission	main reflector emission
15	cold-space mirror emission	cold-space mirror emission
16	warm load emissivity	non-ideal blackbody emissivity, bias
17	spillover	spillover seeing cosmic background
18	FOV intrusion	field of view intrusion due to the spacecraft or payloads
19	payload interference	interference from onboard instruments
20	spacecraft attitude offset	roll, pitch, yaw
21	Faraday rotation	Faraday rotation due to ionosphere and Earth magnetic field
22	count to antenna temperature	calibration frequency, windowing function, etc
23	antenna pattern correction	calibrating antenna temperature to brightness temperature
24	gain and noise long-term change	long-term degradation in terms of noise and gain
25	frequency drift	channel center frequency drift
26	orbit drift	long-term satellite altitude change
27	horizontal spatial correlation	FOV overlap horizontally
28	vertical spatial correlation	vertical overlap of channel weighting functions
29	surface and atmospheric profiles uncertainties	error in surface and atmospheric profiles
30	RTM error	RTM deficiencies in surface, atmospheric models
31	spatial resolution in RTM	vertical or horizontal resolutions affecting RTM simulation
32	collocation	collocation criteria for single or multiple satellite
33	intercalibration	errors due to sensor difference in frequency, scanning angle, collocation criteria, RTM

34	pre-screening	filtering and screening for satellite data
35	retrieval	inversion based retrieval affecting EDR and CDR
36	external models, algorithms	combining our simulator with external RTM, retrieval algorithms

## C List of Scripts

Script Name	Script Name
imp:	polanglecoeff_cross.m
errsat_imp_1fadjust.m	polmix_cross.m
errsat_imp_1fper.m	stokes_refl_conical.m
errsat_imp_attitudeoffset.m	stokes_refl_ct.m
errsat_imp_band2chan_inout.m	
errsat_imp_band2chan.m	prof:
errsat_imp_band2chan_sat_ana.m	col_prof2grid.m
errsat_imp_conic_mirrorcold.m	col_prof2grid_twice.m
errsat_imp_count.m	col_uniquegrid.m
errsat_imp_crosspol.m	ECMWF_pres_sfc2atm_L137.m
errsat_imp_crosstalk.m	ECMWF_pres_sfc2atm_L91.m
errsat_imp_faradayangle.m	ec_read_era5_ana_ml_137_sfc_umd.m
errsat_imp_faradaystokes.m	filter_landmask.m
errsat_imp_farfieldTB_fun.m	ind_filter1D.m
errsat_imp_farfieldTB.m	ind_startend_bin.m
errsat_imp_file_more_count.m	ind_startend_cum.m
errsat_imp_file_simorbit.m	interp_lin_2D_asc.m
errsat_imp_fovaer.m	interp_lin_3D_asc.m
errsat_imp_fovintrusion.m	movingavg_2Dwin_1conv.m
errsat_imp_initcw.m	parse_sensorname.m
errsat_imp_interference.m	prof_atmsfc.m
errsat_imp_loadgranuel.m	prof_interp_atm.m
errsat_imp_noiseadditive.m	prof_read_4sim_bin.m
errsat_imp_noisePRT.m	prof_read_4sim_mat.m
errsat_imp_noiserng.m	prof_write_4sim_bin.m
errsat_imp_nonlinearata.m	prof_write_4sim_mat.m
errsat_imp_orbit.m	prof_write_4sim_nc.m
errsat_imp_orbitsscanning.m	prof_write_dailyinfo.m
errsat_imp_orbitsingle.m	qsub_matlab_one.m
errsat_imp_oscil_gain.m	read_bin_AMSU_A.m
errsat_imp_oscil_PRT.m	read_bin_KLM_MHS_L1B.m
errsat_imp_oscil_tr.m	read_bin_MHS.m
errsat_imp_poisson.m	read_data_cal_tatb_filesdaily.m
errsat_imp_poloffset.m	read_hdf5_atms_daily_geo.m
errsat_imp_prof_files2orbit.m	read_hdf5_atms_daily_sdr_geo.m
errsat_imp_prof_filesca.m	read_hdf5_atms_daily_sdr.m
errsat_imp_prof_files.m	read_hdf5_atms_daily_tdr.m
errsat_imp_prof_filessat.m	read_hdf5_atms_sdr_geo.m
errsat_imp_prof_filessimgran.m	read_sat_filesdaily.m

errsat_imp_prof_flessimorbit.m	read_sim_filesdaily.m
errsat_imp_prof_ini.m	scp_qsub.m
errsat_imp_prof_load.m	set_data_sim_filedaily.m
errsat_imp_prof_read4singleorbit.m	set_FileDaily.m
errsat_imp_receiver.m	set_Read1File.m
errsat_imp_receiverpre_tas.m	ucar_read_era5_ana_pl_37_sfc_umd.m
errsat_imp_receiverpre_tcw.m	write_CRTM_bin_prof.m
errsat_imp_refl_tacw.m	
errsat_imp_refl_tas.m	radcal:
errsat_imp_ref.m	cal2point_win.m
errsat_imp_rtm_atm.m	errsat_cal_2point.m
errsat_imp_save_A.m	errsat_cal_conic_faraday.m
errsat_imp_save_B.m	errsat_cal_conic_fovintrusion.m
errsat_imp_scanning_1fromscanset.m	errsat_cal_conic_mirrorcold.m
errsat_imp_scanning_2fromobsretr.m	errsat_cal_conic_refl_main.m
errsat_imp_scanning_3combo.m	errsat_cal_conic_xpol.m
errsat_imp_scanning_4allfromobs.m	errsat_cal_count2ta.m
errsat_imp_scanning.m	errsat_cal_crosschan.m
errsat_imp_simioout.m	errsat_cal_crosstalk.m
errsat_imp_simioout_more_count.m	errsat_cal_ct_refl_main.m
errsat_imp_simioout_more_toatb.m	errsat_cal_ct_xpol.m
errsat_imp_simiooutpre.m	errsat_cal_interference.m
errsat_imp_simreceiver.m	errsat_cal_nedt.m
errsat_imp_spillover.m	errsat_cal_nonlinear.m
errsat_imp_sr.m	errsat_cal_output.m
errsat_imp_targetTB.m	errsat_cal_output_more.m
errsat_imp_targetTB_prof.m	errsat_cal_output_save.m
errsat_imp_TB_mainsidespillover.m	errsat_cal_output_save_more.m
errsat_imp_TBsource_sidelobe.m	errsat_cal_para_customize.m
errsat_imp_TBsourcesim_load.m	errsat_cal_para_fromsim.m
errsat_imp_TBsourcesim_model.m	errsat_cal_para.m
errsat_imp_TBsource_waveform.m	errsat_cal_para_parse_spillover.m
errsat_imp_TOAtb.m	errsat_cal_read_count.m
errsat_imp_uniqfreq.m	errsat_cal_read_counttatb_less.m
errsat_imp_warmloaderror.m	errsat_cal_read_counttatb_less_setting.m
	errsat_cal_read_counttatb_more.m
intercal:	errsat_cal_read_counttatb_more_setting.m
errsat_3intercal_dd.m	errsat_cal_spillover.m
errsat_3intercal_dd_plot.m	errsat_cal_ta2tb.m
errsat_3intercal_oo.m	errsat_cal_warmloaderror.m
errsat_3intercal_oo_plot.m	errsat_plot_count.m
errsat_3intercal_sd.m	errsat_plot_faraday.m
errsat_3intercal_sd_plot.m	errsat_plot_map_scene.m
errsat_intercal_dd_collocate.m	errsat_plot_nedt.m
errsat_intercal_dd_filter.m	errsat_plot_noiseacf.m
errsat_intercal_dd_output.m	errsat_plot_noisezca.m
errsat_intercal_dd_process.m	errsat_plot_noisepsd.m

errsat_intercal_dd_setting.m	errsat_plot_scandep.m
errsat_intercal_dd_stats.m	errsat_plot_tabias.m
errsat_intercal_oo_collocate.m	errsat_plot_ta.m
errsat_intercal_oo_filter.m	errsat_plot_tanoise.m
errsat_intercal_oo_output.m	
errsat_intercal_oo_process.m	reananlyses:
errsat_intercal_oo_setting.m	ec_main_write_era5_ana_ml_137_sfc_umd.m
errsat_intercal_oo_stats.m	ec_read_era5_ana_ml_137.m
errsat_intercal_plot_sd.m	ec_read_era5_ana_ml_137_sfc_umd.m
errsat_intercal_sd_output.m	ec_read_era5_ana_sfc.m
errsat_intercal_sd_process.m	ec_write_era5_ana_ml_137_sfc_umd.m
errsat_intercal_sd_setting.m	main_era5.py
orbit_period2sat.m	mod_date.py
plot_crosstrack_dd.m	mod_era5_dn.py
plot_crosstrack_oo.m	scaleoffset.m
plot_crosstrack_sd.m	ucar_clw_main_write_era5_ana_pl_37_sfc_umd.m
plot_hist1_dd.m	ucar_clw_read_era5_ana_pl_37_sfc_ucar.m
plot_hist1_oo.m	ucar_clw_read_era5_ana_pl_37_sfc_umd.m
plot_hist1_sd.m	ucar_clw_write_era5_ana_pl_37_sfc_umd.m
plot_hist2_tb_dd.m	
plot_hist2_tb_dif.m	rtm:
plot_hist2_tb_sd.m	atm_6prof.m
plot_map_tb_dd.m	atm_ph_139.m
plot_map_tb_dif.m	humconvert.m
plot_map_tb_sd.m	press2h_interp.m
rad_spc_set.m	rtm_abs_liq.m
xcold_1obs.m	rtm_abs_N2.m
xcold_1obssim.m	rtm_abs_O2.m
xcold_2cal_more.m	rtm_abs_wvp.m
	rtm_atm_abs.m
main:	rtm_atm_updnwell_profmult.m
errsat_main_1sim_imp.m	rtm_atm_updnwell_profone.m
errsat_main_1sim.m	rtm_prof.m
errsat_main_1sim_more_count.m	rtm_tbupdn.m
errsat_main_1sim_more_granule2orbit.m	rtm_toa.m
errsat_main_1sim_more_profcollocate.m	
errsat_main_1sim_more_prof.m	set:
errsat_main_1sim_more_prof_queue.m	errsat_set_antennapattern.m
errsat_main_2cal_less.m	errsat_set_attitudeoffset.m
errsat_main_2cal.m	errsat_set_conic_mirrorcold.m
errsat_main_2cal_more_1cal.m	errsat_set_crosspol.m
errsat_main_2cal_more_2plot.m	errsat_set_crosstalk.m
errsat_main_3intercal.m	errsat_set_faraday.m
errsat_main_retrieval.m	errsat_set_farfieldTB.m
errsat_main_setting.m	errsat_set_fovintrusion.m
errsat_profcollocate.m	errsat_set_georbit_kepler.m
	errsat_set_georbit.m

noise:  
 allandev\_2sample\_2D.m  
 decomp\_NEDT\_1D.m  
 decomp\_NEDT\_2D.m  
 errsat\_noise\_fft1.m  
 errsat\_noise\_poisson.m  
 errsat\_noise\_scale.m  
 errsat\_noise\_sim\_sub.m  
 errsat\_noise\_source.m  
  
 orbit:  
 ang2enu.m  
 ang2ned.m  
 coscan2az.m  
 ctscan2az.m  
 ctscan2enu.m  
 ctscan2tilt.m  
 earth\_wgs84.m  
 enu2ang.m  
 enuo2gc.m  
 eulerrotate.m  
 gc2gd.m  
 gco2enu.m  
 gd2gc.m  
 gd\_linesightx\_ned\_ell.m  
 gd\_linesightx\_ned.m  
 interlos.m  
 ned2ang.m  
 orbit\_kepler.m  
 orbit\_scan2gd\_co.m  
 orbit\_scan2gd\_ct.m  
 scan2ned.m  
 scfov2scaninterp.m  
 scfov2scaninterp\_scheme2.m  
 scfov2scan.m  
 scfov2scan\_scheme2.m  
 scgeo2scaz.m  
 scgeointerp.m  
 sphere\_eia2nadir.m  
 sphere\_nadir2eia.m  
 xenu2ned.m  
  
 others:  
 igrf  
  
 parse:  
 errsat\_parse\_antennapattern.m

errsat\_set\_georbit\_real\_allfromobs.m  
 errsat\_set\_georbit\_real\_scfov.m  
 errsat\_set\_georbit\_real\_sc.m  
 errsat\_set\_interference.m  
 errsat\_set\_jump.m  
 errsat\_set\_modefarfieldTB.m  
 errsat\_set\_noiseadditive\_cust.m  
 errsat\_set\_noiseadditive.m  
 errsat\_set\_noiseadditive\_sensor.m  
 errsat\_set\_noisePRT.m  
 errsat\_set\_noiserng.m  
 errsat\_set\_noisesigdep.m  
 errsat\_set\_nonlinear.m  
 errsat\_set\_oscil.m  
 errsat\_set\_oscil\_sub\_cust.m  
 errsat\_set\_oscil\_sub\_demo.m  
 errsat\_set\_oscil\_sub\_sensor.m  
 errsat\_set\_oscil\_sub\_sensor\_table.m  
 errsat\_set\_path\_scheme.m  
 errsat\_set\_poloffset.m  
 errsat\_set\_profile.m  
 errsat\_set\_rad\_fe.m  
 errsat\_set\_radspc\_adv.m  
 errsat\_set\_radspc\_chan.m  
 errsat\_set\_radspc.m  
 errsat\_set\_rad\_sr.m  
 errsat\_set\_reflcoeff.m  
 errsat\_set\_reflcoeff\_sat\_ana.m  
 errsat\_set\_review.m  
 errsat\_set\_scanning.m  
 errsat\_set\_TBsource.m  
 errsat\_set\_TBsource\_sidelobe.m  
 errsat\_set\_tmpdep.m  
 errsat\_set\_warmloaderror.m  
  
 utility:  
 coeff\_crosstalk\_corr.m  
 dist\_earthxy.m  
 errsat\_const.m  
 errsat\_plot\_obsdaily.m  
 filter\_clwc\_183.m  
 filter\_precip\_land.m  
 filter\_precip\_ocean.m  
 idx\_orbit\_ascdes.m  
 ind\_startend\_2ind.m  
 ind\_startend\_bin.m  
 ind\_startend\_binnun.m

errsat_parse_attitudeoffset.m	ind_startend_cum.m
errsat_parse_conic_mirrorcold.m	interp_lin_2D_asc.m
errsat_parse_crosspol.m	math_window.m
errsat_parse_crosstalk.m	movingavg_cal.m
errsat_parse_faraday.m	movingavg_edge_lr.m
errsat_parse_farfieldTB.m	movingavg_idx_1D.m
errsat_parse_fovintrusion.m	mtimes_2d3d.m
errsat_parse_fovintrusionsub.m	mtimes_3d3d.m
errsat_parse_georbit_kepler.m	ocean_emissivity.m
errsat_parse_georbit_real_scfov.m	pca_svds.m
errsat_parse_georbit_real_sc.m	plot_colormap_whitejet.m
errsat_parse_granuel.m	plot_map_coastline.m
errsat_parse_indCT.m	plot_map_lonedgenan.m
errsat_parse_input.m	plot_map_tb_ascdes.m
errsat_parse_interference.m	plot_subplotnum.m
errsat_parse_no_alongtrack.m	plot_subplotnum_rectangle.m
errsat_parse_noiseadditive_cust.m	polyfitweighted.m
errsat_parse_noiseadditive.m	read_bin_KLM_MHS_L1B.m
errsat_parse_noiseadditive_sensor.m	read_MHS_chan1_89GHz.m
errsat_parse_nonlinear.m	retr_clwc_amsua.m
errsat_parse_orbit.m	retr_tmp_atms.m
errsat_parse_path_scheme.m	retr_wind_ssmi.m
errsat_parse_poloffset.m	scan_ind2ang.m
errsat_parse_profile.m	scanpos2angle.m
errsat_parse_radspc_chan.m	stat_stdhist.m
errsat_parse_radspc.m	sub_collocate.m
errsat_parse_rad_sr.m	sub_filterInd1D.m
errsat_parse_reflcmis.m	sub_filterInd2D.m
errsat_parse_reflcmis_sat_ana.m	sub_gridMapMean_vargrid.m
errsat_parse_scanning.m	sub_hist2.m
errsat_parse_TBsource.m	sub_plotCrossSubChan.m
errsat_parse_warmloaderror.m	sub_plotDirectHist2DFit.m
pol:	sub_uniqmean.m
mueller_refl_ct.m	sub_uniqmeanstd.m

## References

- Nasa global precipitation measurement (gpm) microwave imager (gmi) level 1b (l1b), *Algorithm Theoretical Basis Document (ATBD)*, 2016.
- Ablain, M., et al., Improved sea level record over the satellite altimetry era (1993–2010) from the climate change initiative project, *Ocean Science*, 11(1), 67–82, 2015.
- Alquaied, F., R. Chen, and W. L. Jones, Hot load temperature correction for trmm microwave imager in the legacy brightness temperature, *IEEE Journal of Selected Topics in Applied Earth Observations and Remote Sensing*, 11(6), 1923–1931, 2018.

- Balanis, C., *Antenna theory: Analysis and design*, 318, 2016.
- Balanis, C. A., *Antenna theory: analysis and design*, John Wiley & sons, 2015.
- Bellprat, O., F. Massonnet, S. Siegert, C. Prodhomme, D. Macias-Gómez, V. Guemas, and F. Doblas-Reyes, Uncertainty propagation in observational references to climate model scales, *Remote Sensing of Environment*, 203, 101–108, 2017.
- Bilitza, D., D. Altadill, V. Truhlik, V. Shubin, I. Galkin, B. Reinisch, and X. Huang, International reference ionosphere 2016: From ionospheric climate to real-time weather predictions, *Space weather*, 15(2), 418–429, 2017.
- Bormann, N., and P. Bauer, Estimates of spatial and interchannel observation-error characteristics for current sounder radiances for numerical weather prediction. i: Methods and application to atovs data, *Quarterly Journal of the Royal Meteorological Society*, 136(649), 1036–1050, 2010.
- Cai, G., B. M. Chen, and T. H. Lee, *Unmanned rotorcraft systems*, Springer Science & Business Media, 2011.
- Colton, M. C., and G. A. Poe, Intersensor calibration of dmsp ssm/i’s: F-8 to f-14, 1987-1997, *IEEE Transactions on Geoscience and Remote Sensing*, 37(1), 418–439, 1999.
- Corbella, I., A. J. Gasiewski, M. Klein, V. Leuski, A. J. Francavilla, and J. R. Piepmeier, On-board accurate calibration of dual-channel radiometers using internal and external references, *IEEE transactions on microwave theory and techniques*, 50(7), 1816–1820, 2002.
- Davis, W. A., and K. K. Agarwal, *Radio Frequency Circuit Design*, 2nd ed., Wiley, New York, doi:10.1002/0471200689, 2011.
- Desroziers, G., L. Berre, B. Chapnik, and P. Poli, Diagnosis of observation, background and analysis-error statistics in observation space, *Quarterly Journal of the Royal Meteorological Society: A journal of the atmospheric sciences, applied meteorology and physical oceanography*, 131(613), 3385–3396, 2005.
- Draper, D. W., D. A. Newell, F. J. Wentz, S. Krimchansky, and G. M. Skofronick-Jackson, The global precipitation measurement (gpm) microwave imager (gmi): Instrument overview and early on-orbit performance, *IEEE Journal of Selected Topics in Applied Earth Observations and Remote Sensing*, 8(7), 3452–3462, 2015.
- Geer, A. J., et al., All-sky satellite data assimilation at operational weather forecasting centres, *Quarterly Journal of the Royal Meteorological Society*, 144(713), 1191–1217, 2018.
- Goodberlet, M., C. Swift, and J. Wilkerson, Remote sensing of ocean surface winds with the special sensor microwave/imager, *Journal of Geophysical Research: Oceans*, 94(C10), 14,547–14,555, 1989.
- Gopalan, K., W. L. Jones, S. Biswas, S. Bilanow, T. Wilheit, and T. Kasparis, A time-varying radiometric bias correction for the trmm microwave imager, *IEEE transactions on geoscience and remote sensing*, 47(11), 3722–3730, 2009.
- Griffin, M. D., *Space vehicle design*, AIAA, 2004.

- Gruber, A., et al., Validation practices for satellite soil moisture retrievals: What are (the) errors?, *Remote sensing of environment*, 244, 111,806, 2020.
- Hollingsworth, A., and P. Lönnberg, The statistical structure of short-range forecast errors as determined from radiosonde data. part i: The wind field, *Tellus A*, 38(2), 111–136, 1986.
- Hollmann, R., et al., The esa climate change initiative: Satellite data records for essential climate variables, *Bulletin of the American Meteorological Society*, 94(10), 1541–1552, 2013.
- Janjić, T., et al., On the representation error in data assimilation, *Quarterly Journal of the Royal Meteorological Society*, 144(713), 1257–1278, 2018.
- Joo, S., J. Eyre, and R. Marriott, The impact of metop and other satellite data within the met office global nwp system using an adjoint-based sensitivity method, *Monthly weather review*, 141(10), 3331–3342, 2013.
- Kalnay, E., *Atmospheric modeling, data assimilation and predictability*, Cambridge university press, 2003.
- Kim, E., C.-H. J. Lyu, K. Anderson, R. Vincent Leslie, and W. J. Blackwell, S-npp atms instrument prelaunch and on-orbit performance evaluation, *Journal of Geophysical Research: Atmospheres*, 119(9), 5653–5670, 2014.
- Kroodsmma, R. A., D. S. McKague, and C. S. Ruf, Inter-calibration of microwave radiometers using the vicarious cold calibration double difference method, *IEEE Journal of Selected Topics in Applied Earth Observations and Remote Sensing*, 5(3), 1006–1013, 2012.
- Kuan, D. T., A. A. Sawchuk, T. C. Strand, and P. Chavel, Adaptive noise smoothing filter for images with signal-dependent noise, *IEEE transactions on pattern analysis and machine intelligence*, (2), 165–177, 1985.
- Langland, R. H., and N. L. Baker, Estimation of observation impact using the nrl atmospheric variational data assimilation adjoint system, *Tellus A: Dynamic Meteorology and Oceanography*, 56(3), 189–201, 2004.
- Lee, T. H., *The Design of CMOS Radio-Frequency Integrated Circuits*, Cambridge Univ, doi:10.1017/cbo9780511817281, 2004.
- Matsumoto, M., and T. Nishimura, Mersenne twister: a 623-dimensionally equidistributed uniform pseudo-random number generator, *ACM Transactions on Modeling and Computer Simulation (TOMACS)*, 8(1), 3–30, 1998.
- McKague, D. S., C. S. Ruf, and J. J. Puckett, Beam spoiling correction for spaceborne microwave radiometers using the two-point vicarious calibration method, *IEEE transactions on geoscience and remote sensing*, 49(1), 21–27, 2010.
- Meissner, T., and F. J. Wentz, Polarization rotation and the third stokes parameter: The effects of spacecraft attitude and faraday rotation, *IEEE Transactions on Geoscience and Remote Sensing*, 44(3), 506–515, 2006.
- Merchant, C. J., et al., Uncertainty information in climate data records from earth observation, *Earth System Science Data*, 9(2), 511–527, 2017.



- Merchant, C. J., et al., Satellite-based time-series of sea-surface temperature since 1981 for climate applications, *Scientific data*, 6(1), 1–18, 2019.
- Mo, T., Prelaunch calibration of the advanced microwave sounding unit-A for NOAA-K, *IEEE Transactions on Microwave theory and Techniques*, 44(8), 1460–1469, 1996.
- Peng, J., et al., Soil moisture active/passive l-band microwave radiometer postlaunch calibration, *IEEE Transactions on Geoscience and Remote Sensing*, 55(9), 5339–5354, 2017.
- Riley, W. J., Nist special publication 1065, *Handbook of frequency stability analysis*, p. 60, 2008.
- Robel, J., and A. Graumann, Noaa klm user’s guide with noaa-n, *N Prime, and MetOp SUPPLEMENT*: <https://www.nasa.gov/pdf/111742main-noaa-n-booklet.pdf>, 2014.
- Rosenkranz, P., Line-by-line microwave radiative transfer (non-scattering), *Remote Sensing Code Library*, [https://doi.org/10.21982/M\\_81013](https://doi.org/10.21982/M_81013), 2017.
- Rosenkranz, P. W., Cloud liquid-water profile retrieval algorithm and validation, *Journal of Geophysical Research: Atmospheres*, 111(D9), 2006.
- Rosenkranz, P. W., and D. Cimini, Speed dependence of 22-and 118-ghz line shapes for tropospheric remote sensing, *IEEE Transactions on Geoscience and Remote Sensing*, 57(12), 9702–9708, 2019.
- Ruf, C. S., Constraints on the polarization purity of a stokes microwave radiometer, *Radio Science*, 33(6), 1617–1639, 1998.
- Schiek, B., H.-J. Siweris, and I. Rolfes, *Noise in high-frequency circuits and oscillators*, John Wiley & Sons, 2006.
- Stewart, L., S. L. Dance, N. K. Nichols, J. Eyre, and J. Cameron, Estimating interchannel observation-error correlations for iasi radiance data in the met office system, *Quarterly Journal of the Royal Meteorological Society*, 140(681), 1236–1244, 2014.
- Sullivan, D. B., D. W. Allan, D. A. Howe, and F. L. Walls, *Characterization of clocks and oscillators*, National Institute of Standards and Technology Technical Note, 1990.
- Thébault, E., et al., International geomagnetic reference field: the 12th generation, *Earth, Planets and Space*, 67(1), 1–19, 2015.
- Twarog, E. M., W. E. Purdy, P. W. Gaiser, K. H. Cheung, and B. E. Kelm, Windsat on-orbit warm load calibration, *IEEE Transactions on Geoscience and Remote Sensing*, 44(3), 516–529, 2006.
- Ulaby, F. T., D. G. Long, W. J. Blackwell, C. Elachi, A. K. Fung, C. Ruf, K. Sarabandi, H. A. Zebker, and J. Van Zyl, *Microwave radar and radiometric remote sensing*, vol. 4, University of Michigan Press Ann Arbor, 2014.
- Vasilescu, G., *Electronic noise and interfering signals: principles and applications*, Springer Science & Business Media, 2005.
- Weng, F., X. Zou, N. Sun, H. Yang, M. Tian, W. J. Blackwell, X. Wang, L. Lin, and K. Anderson, Calibration of suomi national polar-orbiting partnership advanced technology microwave sounder, *Journal of Geophysical Research: Atmospheres*, 118(19), 11–187, 2013.

- Wentz, F. J., and D. Draper, On-orbit absolute calibration of the global precipitation measurement microwave imager, *Journal of Atmospheric and Oceanic Technology*, 33(7), 1393–1412, 2016.
- Wentz, F. J., P. Ashcroft, and C. Gentemann, Post-launch calibration of the trmm microwave imager, *IEEE Transactions on Geoscience and Remote Sensing*, 39(2), 415–422, 2001.
- Weston, P., W. Bell, and J. Eyre, Accounting for correlated error in the assimilation of high-resolution sounder data, *Quarterly Journal of the Royal Meteorological Society*, 140(685), 2420–2429, 2014.
- Yang, J. X., and H. Yang, Radiometry calibration with high-resolution profiles of gpm: Application to atms 183-ghz water vapor channels and comparison against reanalysis profiles, *IEEE Transactions on Geoscience and Remote Sensing*, 57(2), 829–838, 2018.
- Yang, J. X., D. S. McKague, and C. S. Ruf, Uncertainties in radiometer intercalibration associated with variability in geophysical parameters, *Journal of Geophysical Research: Atmospheres*, 121(19), 11–348, 2016.
- Zhu, T., and F. Weng, Hurricane sandy warm-core structure observed from advanced technology microwave sounder, *Geophysical Research Letters*, 40(12), 3325–3330, 2013.